

# AISAN TECHNICAL JOURNAL

Special  
Feature

Carbon Neutrality



# AISAN TECHNICAL JOURNAL

## Special Feature: Carbon Neutrality

### Contents

#### Opening Message

“Beaming Future by Environmental Technologies” .....	P.02
--	------

#### Special Feature: Carbon Neutrality

##### Papers

- Numerical Adsorption Simulation of Low-Concentration Ammonia... P.04
- Research and Development of Ambient-Temperature Hydrogenation Technology for Low-Energy Startup of Ammonia Power Generation ... P.09
- Development of the Fuel Tank Closed Valve using a stepping motor ... P.13

##### Initiatives

- Change in the Resin Material Used for Canisters ..... P.17

##### Award-Winning Technologies

- Electric Pump That Works with Carbon Neutral Fuels ..... P.19
- Air Control Valve for Fuel Cell Systems ..... P.22

#### General Entries

##### Papers

- Proposal of Phase Shedding Control System for Multiphase PFC Converter ..... P.24
- Estimating the gate-source voltage inside the device ..... P.28
- Development and Practical Application of ADC12 Aluminum Alloy Semi-Solid Die Casting Mass Production Technology Using Mechanical Vibration ..... P.32

##### Initiatives

- Motor Controller for Small Mobility ..... P.37
- Deep Drawing Technology Development for BEV Battery Cases..... P.39
- Developing Software Engineers for Vehicle Electrification..... P.41
- MBD Promotion through Model Libraries ..... P.43
- Solenoid Valve Development through Coupled Analysis..... P.45
- Join the Intellectual Property Business Matching Projects ..... P.47

##### Award-Winning Technologies

- Double Eccentric Valve for EGR Systems ..... P.49

All content published in this technical journal, including photographs, diagrams, illustrations, etc., is protected by copyright law. Unauthorized reproduction, duplication, or redistribution is strictly prohibited.

If you wish to reproduce or use any of this content, please contact us at the following URL:

<https://www.aisan-ind.co.jp/contact/index.htm>

# “Beaming Future by Environmental Technologies”



Akihiro Yamanaka

Vice President

In recent years, frequent and devastating disasters have occurred around the world due to global climate change. One potential cause of this phenomenon is global warming, which is believed to be caused by greenhouse gases, such as CO<sub>2</sub> and methane. These environmental issues have long been recognized, and various efforts have been made to address them.

In the United States, the social issue of air pollution in urban areas led to the enactment of the Clean Air Act in 1963 and its subsequent amendment in 1970, more commonly referred to as the Muskie Act. The amended act was very strict and greatly impacted the development of environmental technologies for cars. Following the first oil crisis triggered by the Yom Kippur War in 1973, which caused oil prices to skyrocket, countries began implementing regulations to improve the fuel efficiency in cars, which promoted energy conservation. Consequently, while CO<sub>2</sub> emissions per car were mitigated, the aggregate amount of CO<sub>2</sub> emissions continued to rise in tandem with global economic expansion.

The 1992 United Nations Conference on Environment and Development (Earth Summit), held in Rio de Janeiro, Brazil, is widely regarded as a significant turning point in thinking about global environmental issues. At this conference, initiatives to achieve “sustainable development” that balances the environment and development were discussed, and the United Nations Framework Convention on Climate Change was adopted.

Then, in 1997, the Kyoto Protocol was adopted at the Third Conference of the Parties (COP3) to the United Nations Framework Convention on Climate Change held in Kyoto.

This protocol set reduction targets for greenhouse gas emissions in developed countries. In response to this change, Japan began mass-producing hybrid cars, which were twice as fuel efficient as conventional cars. This sparked a global increase in the development of various electrified vehicles.

Furthermore, the Paris Agreement was adopted at the 2015 United Nations Climate Change Conference (COP21). Its goal is to “keep the global average temperature rise well below 2°C above pre-industrial levels and pursue efforts to limit the temperature increase to 1.5°C.” The agreement stipulates that the world aims to achieve “decarbonization.” This means that global greenhouse gas emissions will be reduced to net zero in the second half of this century. This goal is based on scientific evidence presented by the Intergovernmental Panel on Climate Change (IPCC).

In Japan, "carbon neutrality," the feature theme of this technical journal, was declared by the prime minister in 2020. The goal is to reduce greenhouse gas emissions to zero overall by the year 2050.

As mentioned earlier, strict regulations about car emissions and fuel efficiency have been gradually introduced in various countries to improve the environment. Technologies to meet these regulations have also evolved. Moreover, the new “zero CO<sub>2</sub>” goal has been added and has led to quick changes. In recent years, many cars with internal combustion engines have been replaced by electric vehicles.

However, electric vehicles are expensive, and the current methods of generating the electricity needed to charge them rely on fossil fuels, making them far from clean. Also, it's hard to solve problems like not having enough charging stations, charging taking a long time, and the cars not being able to drive very far on one charge. This is causing the extreme shift toward electric vehicles to slow down somewhat.

Of course, the goal of achieving zero CO<sub>2</sub> emissions hasn't changed. However, instead of solely seeking solutions through switching to electric vehicles, we believe it is important to combine various types of vehicles with different advantages and respond through multiple pathways. These pathways range from energy conservation and CO<sub>2</sub> reduction to zero CO<sub>2</sub>emissions.

Let's take a look at cars with internal combustion engines. We can achieve zero CO<sub>2</sub> emissions by using carbon-neutral fuels such as biofuels, e-fuels, and hydrogen. In addition, if we eliminate other emissions, such as hydrocarbons (HC) and nitrogen oxides (NOx), these cars can be considered equivalent to electric vehicles that are charged by clean energy. Furthermore, cars with internal combustion engines can also achieve negative emissions by taking in polluted air and purifying it, thereby cleaning the atmosphere.

Aisan has long been involved in developing functional products for internal combustion engines such as air intake systems, fuel supply systems, and exhaust gas control systems. We've also worked on environmental technologies related to fuel efficiency and exhaust gas control and suitability for cars. We are experts especially in fuel supply systems. We can handle many different fuels, including gasoline, LPG, CNG, and alcohol fuels.

We aim to achieve zero CO<sub>2</sub> emissions and zero other emissions from cars with internal combustion engines using these technologies. We also hope to contribute to the protection and preservation of the global environment by expanding these technologies to countries in the Global South and other regions.

Aisan will also use these environmental technologies to develop and produce new technologies related to electrification, clean energy (fuel cells, hydrogen, ammonia, etc.), and new mobility. We will also work to develop software and systems that can work with AI and software-defined vehicles (SDVs) in a way that follows current trends. We aim to help achieve carbon neutrality and solve societal challenges by innovating Aisan strengths in MONOZUKURI and production technologies, as well as providing solutions that create new values.

Lastly, we will continue developing new environmental technologies to help the automotive industry grow and provide high-quality products and services. In doing so, we will contribute to society and help create a beaming future.

# Numerical Adsorption Simulation of Low-Concentration Ammonia

Seiya Kusaka, Tomoyuki Ichikawa, Hiroki Miyaoka, Takayuki Ichikawa

## Abstract

In numerical simulations to predict breakthrough behaviors of a detoxifier to remove trace ammonia remaining in hydrogen produced by ammonia cracking, the equilibrium adsorption amount has been determined from the fitting equation of adsorption isotherm, but for low-concentration gases, the prediction accuracy of breakthrough time is low. In this study, several measurements with varying dose pressure and temperature were carried out to measure the ammonia adsorption isotherms of zeolite that can correspond to low-concentration gas breakthrough experiments. These isotherms were formulated by Roginsky's dispersion function method. This allowed us to predict breakthrough time for low-concentration gas on the order of ppm.

## 1. Introduction

Hydrogen has been gaining attention in recent years due to its environmentally friendly nature and the fact that its heat of combustion per unit mass is the highest among all chemical fuels. However, its critical temperature is extremely low at 33 K, and its critical pressure is also relatively low at 1.3 MPa. As a result, the energy per unit volume of hydrogen is very small at room temperature. Additionally, hydrogen has a wide flammability range of 4% to 75%, making it highly explosive, and its flame is both high-temperature and invisible. Therefore, techniques for storing hydrogen more safely and at higher densities are required.

As means of storing and transporting hydrogen energy, the use of hydrogen compounds such as metal hydrides, ammonia borane, and methylcyclohexane is being explored<sup>(1,2)</sup>. Among these, liquid ammonia has attracted attention due to its ability to liquefy easily at 1 MPa even at room temperature and its high combustion heat per unit volume<sup>(3)</sup>. Furthermore, since the number of hydrogen atoms per unit volume is 1.5 times that of liquid hydrogen, it possesses excellent characteristics as a hydrogen carrier. However, since ammonia has high toxicity and corrosiveness even at low concentrations in the ppm range, any residual ammonia must be removed, whether it is cracked into hydrogen or used directly. In terms of level, when using it as a hydrogen source for polymer electrolyte fuel cells, which are also installed in fuel cell vehicles, the residual ammonia concentration must be reduced to 0.1 ppm or lower to suppress fuel cell degradation caused by poisoning<sup>(4)</sup>. There are various ways to remove ammonia, but adsorption-based decontamination using an adsorbent was adopted as a method capable of handling low-concentration ammonia while allowing for a large processing capacity<sup>(5-9)</sup>. Aisan Industry Co., Ltd. has a proven track record in designing and manufacturing charcoal canisters as gasoline vapor adsorption devices, and

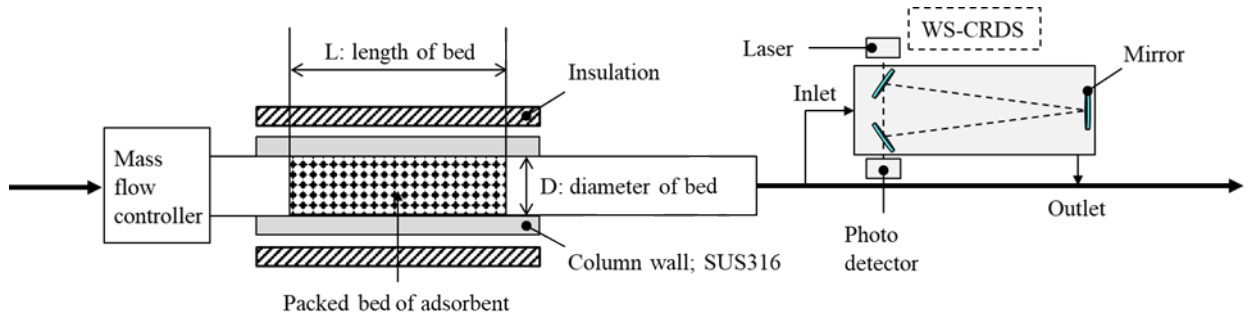
its expertise is also expected to be applicable. An important factor in designing a decontamination device is predicting the breakthrough characteristics, which describe the time dependence of ammonia that flows downstream of the device. Numerous studies have reported the use of numerical simulations to predict the breakthrough characteristics of volatile organic compounds and carbon dioxide adsorption. However, characteristics on the order of ppm have not been examined<sup>(10-14)</sup>. This study focuses on the adsorption behavior of low-concentration ammonia on zeolite and develops a simulation model of an adsorption tower capable of predicting breakthrough characteristics at the ppm level, which are generally difficult to predict.

## 2. Experiment and Simulation

### 2.1. Experimental Method

Various adsorbents are suitable for ammonia adsorption; however, in this study, we used Na-exchanged X-type zeolite (NaX; F9-HA; Tosoh Corporation), which is inexpensive, has a high adsorption capacity, and allows desorption of adsorbed ammonia simply by heating<sup>(15)</sup>. The breakthrough experiment was conducted using the apparatus shown in Figure 1. Most parts of the apparatus were the same as those used in the previous study by Miyaoka et al.<sup>(16)</sup>. The column had an inner diameter of 25 mm, and the zeolite was measured and packed to achieve a packed bed length of 100 mm. The packed bed was fixed using glass wool, a perforated metal plate, and a coil spring. As a pretreatment for the breakthrough experiment, the column was heated to 350°C while flowing argon at 100 L/h until the ammonia concentration meter indicated less than 0.1 ppm, after which it was cooled to the experiment temperature. The ammonia gas mixture used in the experiment was a pre-adjusted gas with a composition ratio of 74.9% hydrogen,

Figure 1 Schematic diagram of breakthrough experiment apparatus



25% nitrogen, and 1000 ppm ammonia. The breakthrough curve represents the time dependence of the ammonia concentration in the gas exiting the column and the residence time.

The ammonia adsorption isotherm was measured using a BELSORP-max (MicrotracBEL). In this apparatus, the sample tube containing zeolite was evacuated, and pure ammonia was dosed in small increments. The amount of adsorption was then calculated based on the equilibrium pressure before and after the dosing of ammonia in the sample tube and the apparatus piping.

## 2.2. Simulation Method

The simulation is based on a model that simultaneously solves the adsorption isotherm, mass conservation law, energy conservation law, and adsorption rate equation. Calculations were performed using Dymola 2017 by Dassault Systems. This model is based on the following assumptions:

- (1) The supplied gas is an ideal gas composed of two components: ammonia and a carrier gas.
- (2) Local thermal equilibrium is assumed, meaning the gas and the adsorbent at a given location have the same temperature.
- (3) The molecular diffusion term in the mass conservation and energy conservation equations is considered negligible compared to the advection term.
- (4) The adsorption rate equation is expressed using the linear driving force approximation.
- (5) Zeolite adsorbs only ammonia, while adsorption of the carrier gas is neglected.
- (6) The initial temperature and pressure within the column are uniform.
- (7) The dependence of physical quantities on the radial direction of the column is ignored.
- (8) The porosity within the column, the bulk density of the adsorbent, and the specific heat capacities of both the column and the adsorbent are constant.

Based on these assumptions, the following set of equations was derived.

The law of mass conservation is expressed as follows:

$$\frac{\partial \rho}{\partial t} = -\frac{\partial(u\rho)}{\partial x} - \frac{\hat{\rho}_z}{\varepsilon} \frac{\partial q}{\partial t} \quad (1)$$

where  $\rho$  (kg/m<sup>3</sup>),  $u$  (m/s),  $t$  (s),  $x$  (m),  $\varepsilon$ ,  $q$  (kg/kg NaX) and  $\hat{\rho}_z$  (kg/m<sup>3</sup>) represent the density of the mixed gas, the

superficial velocity, time, the coordinate along the column axis, the porosity, the amount of ammonia adsorbed per unit mass of zeolite, and the bulk density of the zeolite, respectively.

The law of energy conservation is expressed as follows:

$$C_{p,z} \hat{\rho}_z \frac{\partial T}{\partial t} = -\varepsilon C_{p,g} \rho u \frac{\partial T}{\partial x} + Q_{in} + W \quad (2)$$

where  $C_{p,z}$  (J/kg/K),  $C_{p,g}$  (J/kg/K),  $C_{p,g}$  (J/kg/K),  $T$  (K),  $Q_{in}$  (W/m<sup>3</sup>) and  $W$  (W/m<sup>3</sup>) represent the specific heat of zeolite, the specific heat of the mixed gas, the temperature of the mixed gas, the heat influx from the column wall, and the adsorption heat, respectively.

The adsorption rate equation is given as follows:

$$\frac{\partial q}{\partial t} = k_f \hat{\rho}_{NH_3} \left( \frac{P_{NH_3} - P_{NH_3}^*}{P} \right) \quad (3)$$

where  $\hat{\rho}_{NH_3}$  (kg/m<sup>3</sup>),  $P_{NH_3}^*$  (Pa) and  $P_{NH_3}$  (Pa) represent the density of pure ammonia gas, the interfacial partial pressure of ammonia, and the partial pressure of ammonia, respectively. The interfacial partial pressure of ammonia refers to the hypothetical ammonia partial pressure that would be in equilibrium with the adsorbed amount  $q$ .  $k_f$  is the adsorption rate coefficient, and in this model, Yoshida's equation is adopted<sup>(17)</sup>:

$$(k_f/u)(Sc)^{2/3} \propto [Re/(1-\varepsilon)]^{-0.51} \quad (4)$$

where  $Re$  and  $Sc$  represent the Reynolds number and the Schmidt number, respectively.

The adsorption isotherm expresses the equilibrium relationship between pressure and adsorption amount, which is necessary for determining the interfacial partial pressure of ammonia, and various equation models exist. The Dubinin–Astakhov model<sup>(18)</sup> was used to design the charcoal canister, assuming that gasoline vapor is adsorbed in liquid form. On the other hand, in the case of ultra-low concentration ammonia adsorption, the adsorption amount is small, causing ammonia molecules to be directly adsorbed onto the zeolite surface. Based on previous research on hydrogen adsorption, it is expected that the adsorption state on the outermost surface of the adsorbent will not be able to be considered a liquid<sup>(19)</sup>. Therefore, in this study, a specific adsorption model was adopted. Furthermore, since ammonia, like water, is a polar molecule, previous research by Shirono et al. on water molecule adsorption onto zeolite was also referenced<sup>(20)</sup>. Shirono et al. demonstrated through molecular simulations that NaX zeolite possesses three types of cations, but only two

Figure 2

(a) Adsorption isotherm of ammonia at T = 298 K,  
(b) Breakthrough curve of ammonia at T = 298 K

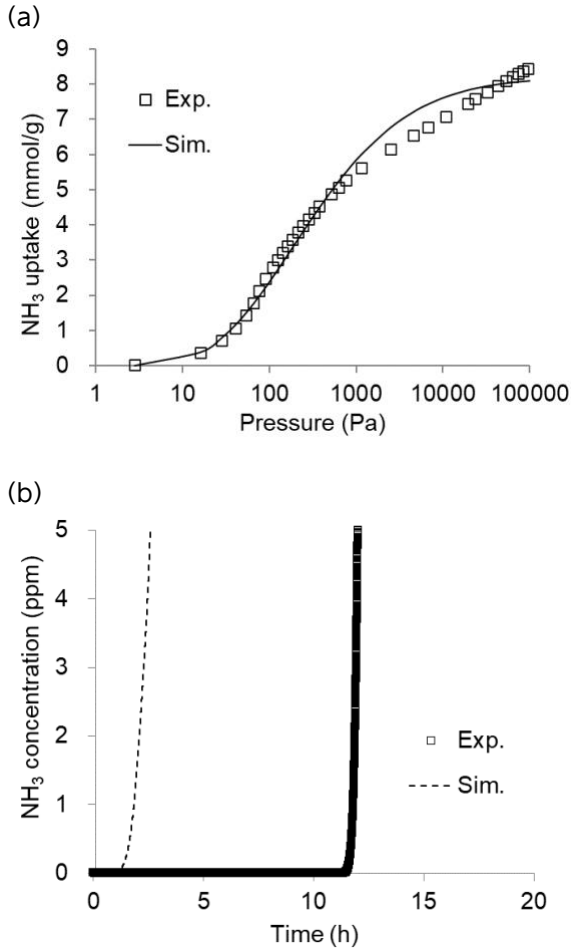
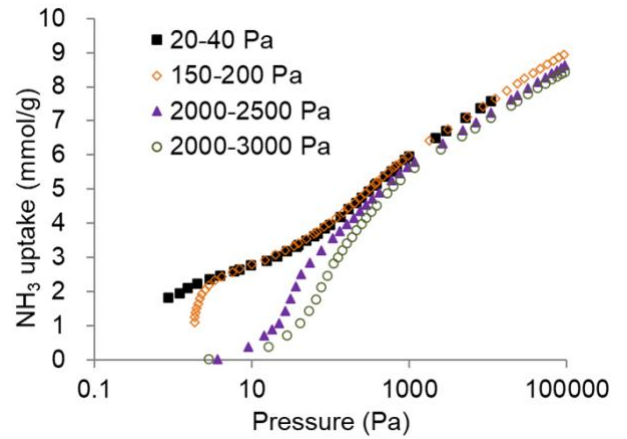


Figure 3

Adsorption isotherm of ammonia measured at  
T = 298 K with varying dosing pressures



$$W = -\frac{1}{\hat{V}_{\text{NH}_3}} \frac{\partial q}{\partial t} [RT \ln K_0 P_{\text{NH}_3}^*] \quad (7)$$

where  $\hat{V}_{\text{NH}_3}$  ( $\text{m}^3/\text{mol}$ ) is the molar volume of pure ammonia gas.

Equation (5) for the adsorption isotherm contains three parameters. However, since predicting these values theoretically is difficult, in practice, the adsorption isotherm is experimentally measured, and the results are fitted to formulate the equation and apply it to the simulation model.

### 3. Results and Discussion

#### 3.1. Exploratory Experiment Results

A mixed gas was supplied to a column filled with zeolite at a flow rate of 275 L/h (stp). The temperature was 298 K, and the pressure was 114 kPa. A numerical simulation was conducted under the same conditions as this experiment to verify the validity of the model. Figure 2a shows the measured adsorption isotherm used in the simulation along with the fitting results, while Figure 2b presents the breakthrough experiment results and the simulation results. In Figure 2b, regardless of the value of the fitting parameter  $k_f$ , the simulation results indicate that the ammonia concentration begins to increase much earlier than the experimental results. This suggests that the amount of adsorption in the simulation is smaller than the actual adsorption amount. Since the adsorption amount in the simulation is determined based on the adsorption isotherm, and the isotherm appears to be well-fitted in Figure 2a, this result implies that the static adsorption amount obtained from the adsorption isotherm measurement and the dynamic adsorption amount obtained from the breakthrough experiment may differ.

Since the breakthrough experiment is conducted using a mixed gas, the total pressure remains above atmospheric pressure even when the partial pressure of ammonia is low. On the other hand, the adsorption isotherm measurement is performed using pure ammonia gas. For realizing the low partial pressure of ammonia, the total pressure should be low.

function as adsorption sites. These two adsorption sites do not interact with ammonia molecules in a one-to-one manner; rather, adsorption can also occur at intermediate positions between the two sites. Taking these factors into account, this study developed a model incorporating specific adsorption heterogeneity, referring to the method by Roginsky et al.<sup>(21)</sup>. The distribution function of adsorption sites follows a Gaussian distribution with respect to adsorption energy. Assuming that this distribution is independent of temperature, the equation for equilibrium adsorption capacity is given as follows:

$$q = q_t \left[ 1 - \frac{1}{2} \text{erfc} \left( -\frac{\tilde{E}}{\sqrt{2}} \right) \right] \quad (5)$$

where  $q_t$  (kg/kg-NaX) represents the maximum adsorption capacity, erfc is the complementary error function, and  $(\tilde{E})$  is given by:

$$\tilde{E} = \frac{-RT \ln K_0 P_{\text{NH}_3}^* - E_0}{\sigma} \quad (6)$$

where  $E_0$ ,  $\sigma^2$ , and  $K_0$  are parameters corresponding to the mode, standard deviation, and equilibrium coefficient, respectively. R is the gas constant. In this model, the adsorption heat is expressed as:

**Figure 4** (a) Adsorption isotherms at various temperatures (plotted points represent measured values, while the solid lines indicate the approximation formula), (b) Distribution of adsorption sites calculated from adsorption isotherms

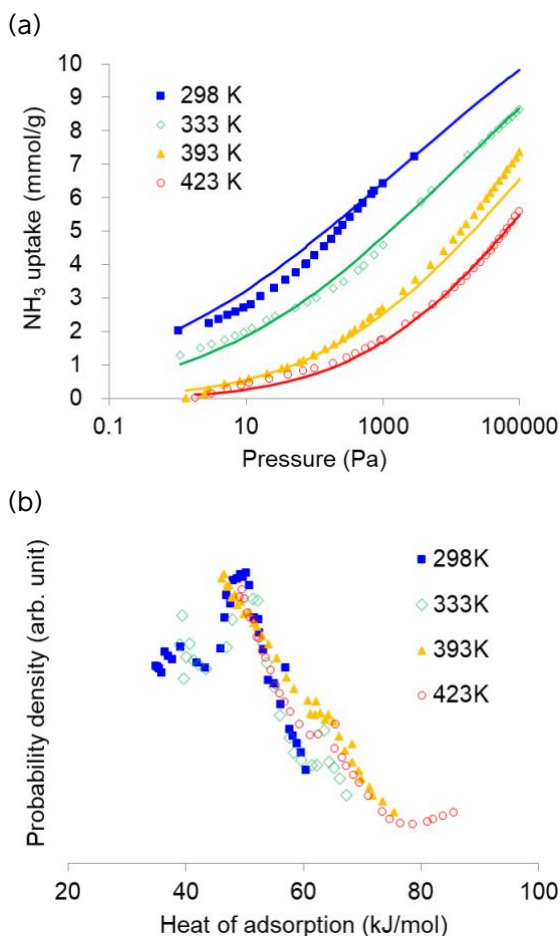
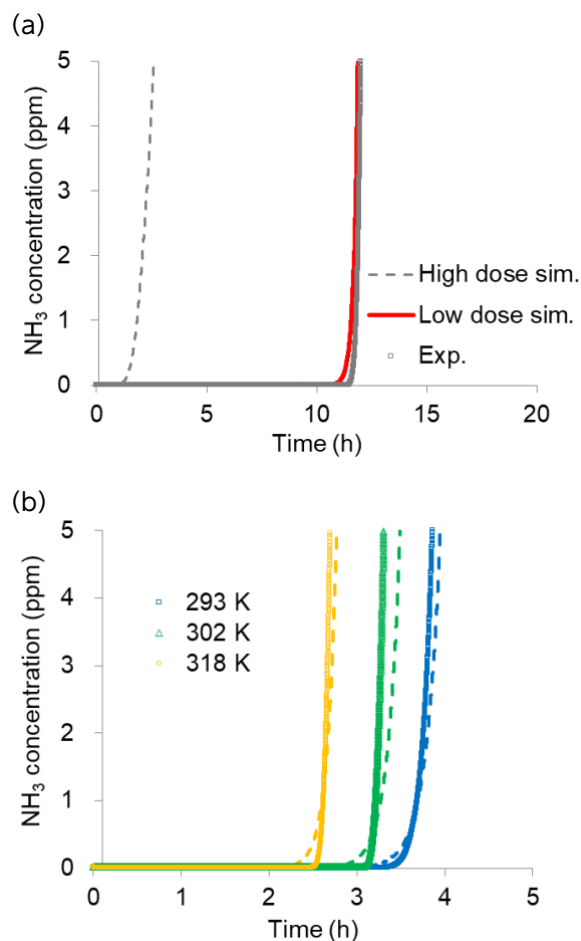


**Figure 5** (a) Breakthrough curve using the improved (Low dose) model, (b) Breakthrough curves at various temperatures. The solid lines indicate measured values, while the dashed lines indicate simulation predictions.



In a previous study by Shirono et al., it was suggested that when water is adsorbed onto zeolite, it may form clusters around adsorption sites<sup>(20)</sup>. Since ammonia, like water, has strong polarity and is considered to form clusters in a similar manner, it is suggested that when the total pressure is low, these clusters prevent ammonia molecules from diffusing into the interior of the zeolite crystal, potentially reaching equilibrium with most adsorption sites remaining unused.

### 3.2. Experiment Results After Modification

Regarding diffusion inhibition, a similar phenomenon has been reported in the hydrogen storage process of palladium-coated magnesium<sup>(22)</sup>. Considering this analogy, the cause of clustering is presumed to be rapid adsorption. Therefore, during the measurement of the adsorption isotherm, an experiment was conducted in which the amount of dosed ammonia was reduced. The results of adsorption isotherm measurements conducted while varying the dosing pressure are shown in Figure 3. From these results, it can be observed that the adsorption amount in the region 10 Pa or below varies significantly depending on the dosing pressure. In the breakthrough experiment, ammonia is thought to have sufficiently diffused into the interior of the zeolite crystals.

Therefore, the adsorption isotherm measured under the smallest dosing pressure, where adsorption is also expected to progress into the interior of the crystals, was deemed suitable for simulation. The results of adsorption isotherm measurements conducted while lowering the dosing pressure and further varying the temperature are shown in Figure 4a. The distribution function of adsorption sites was calculated based on these adsorption isotherms, yielding Figure 4b. This function was then fitted using a Gaussian distribution, formulated, and applied to numerical simulations.

Next, a simulation was conducted under the same conditions as the previous experiment, with a flow rate of 275 L/h (stp), a temperature of 298 K, and a pressure of 114 kPa, to determine the value of the fitting parameter  $k_f$ . As shown in Figure 5a, when the adsorption isotherm measured at a lower inlet pressure was applied to the simulation model, a solution emerged in which the breakthrough characteristics matched the experimental results. To verify the usefulness of the developed simulation model, breakthrough experiments were conducted under different conditions and compared with the simulation predictions. Figure 5b presents the results of a breakthrough experiment performed at a flow rate of 900 L/h (stp) and a pressure of 190 kPa, along with the corresponding

simulation predictions. The time required for a breakthrough concentration of 0.1 ppm was found to match within a margin of error of approximately 10%, even with variations in temperature and flow rate, demonstrating the model's ability to accurately predict breakthrough characteristics even at low ppm-level concentrations. Although the results are omitted here, the model also successfully predicted breakthrough characteristics in experiments where the column inner diameter and packed bed length were varied.

## 4. Conclusion

In this study, an unexpected result was obtained in the measurement of adsorption isotherms using the constant-volume method, where the adsorption amount varied depending on the dosing pressure. Among these adsorption isotherms, simulation results indicated that the isotherm measured at a lower dosing pressure corresponds to the breakthrough experiment. This dosing pressure dependency of the adsorption isotherm suggests the possibility of ammonia molecule clustering, but further detailed investigation is required. Additionally, the newly developed adsorption isotherm model formula is considered applicable to adsorbents with multiple types of adsorption sites and is expected to be useful not only for zeolites but also for other adsorbents such as MOFs and PCPs.

By incorporating two key factors, the measurement of adsorption isotherms corresponding to breakthrough experiments and the formulation of adsorption isotherms considering the heterogeneity of adsorption sites, it has become possible to develop a simulation model that accurately predicts breakthrough characteristics even at low concentrations on the order of ppm. These results can be utilized in techniques for the safe use of ammonia as a hydrogen carrier and are expected to contribute to the realization of a future hydrogen society.

### Reference:

- (1) A. Züttel, Hydrogen storage methods, *Naturwissenschaften* 91 (2004) 157–172. <https://doi.org/10.1007/s00114-004-0516-x>.
- (2) U. Eberle, M. Felderhoff, F. Schüth, Chemical and physical solutions for hydrogen storage, *Angewandte Chemie - International Edition* 48 (2009) 6608–6630. <https://doi.org/10.1002/anie.200806293>.
- (3) A. Valera-Medina, H. Xiao, M. Owen-Jones, W.I.F. David, P.J. Bowen, Ammonia for power, *Prog Energy Combust Sci* 69 (2018) 63–102. <https://doi.org/10.1016/j.pecs.2018.07.001>.
- (4) ISO 14687, Hydrogen fuel quality - Product specification, 2019.
- (5) C.Y. LIU, K. AIKA, Ammonia adsorption on ion exchanged Y-zeolites as ammonia storage material, *Journal of the Japan Petroleum Institute* 46 (2003) 301–307.
- (6) C.C. Rodrigues, D. de Moraes, S.W. da Nóbrega, M.G. Barboza, Ammonia adsorption in a fixed bed of activated carbon, *Bioresour Technol* 98 (2007) 886–891. <https://doi.org/https://doi.org/10.1016/j.biortech.2006.03.024>.
- (7) P. Kumar, K.-H. Kim, E.E. Kwon, J.E. Szulejko, Metal-organic frameworks for the control and management of air quality: advances and future direction, *J Mater Chem A Mater* 4 (2016) 345–361.
- (8) B. Wang, L.H. Xie, X. Wang, X.M. Liu, J. Li, J.R. Li, Applications of metal-organic frameworks for green energy and environment: New advances in adsorptive gas separation, storage and removal, *Green Energy and Environment* 3 (2018) 191–228. <https://doi.org/10.1016/j.gee.2018.03.001>.
- (9) M. Tamotu, B. Keito, T. Seiki, Studies on the adsorption removal of ammonia gas, 2) adsorption of ammonia gas on several kinds of zeolites, *Sangyo Igaku* 19 (1977) 87–91. <https://doi.org/10.1539/joh1959.19.87>.
- (10) R. Ben-Mansour, M.A. Habib, O.E. Bamidele, M. Basha, N.A.A. Qasem, A. Peedikakkal, T. Laoui, M. Ali, Carbon capture by physical adsorption: Materials, experimental investigations and numerical modeling and simulations - A review, *Appl Energy* 161 (2016) 225–255. <https://doi.org/10.1016/j.apenergy.2015.10.011>.
- (11) Y. Xiao, S. Qiu, Q. Zhao, Y. Zhu, C.B. Godiya, G. He, Numerical simulation of low-concentration CO<sub>2</sub> adsorption on fixed bed using finite element analysis, *Chin J Chem Eng* 36 (2021) 47–56. <https://doi.org/10.1016/j.cjche.2020.08.012>.
- (12) J.A. Delgado, M.A. Uguina, J.L. Sotelo, B. Ruiz, Fixed-bed adsorption of carbon dioxide-helium, nitrogen-helium and carbon dioxide-nitrogen mixtures onto silicalite pellets, *Sep Purif Technol* 49 (2006) 91–100. <https://doi.org/10.1016/j.seppur.2005.08.011>.
- (13) D.T. Tefera, M. Jahandar Lashaki, M. Fayaz, Z. Hashisho, J.H. Philips, J.E. Anderson, M. Nichols, Two-dimensional modeling of volatile organic compounds adsorption onto beaded activated carbon, *Environ Sci Technol* 47 (2013) 11700–11710. <https://doi.org/10.1021/es402369u>.
- (14) C.L. Chuang, P.C. Chiang, E.E. Chang, Modeling VOCs adsorption onto activated carbon, *Chemosphere* 53 (2003) 17–27. [https://doi.org/10.1016/S0045-6535\(03\)00357-6](https://doi.org/10.1016/S0045-6535(03)00357-6).
- (15) S.H. Satoshi YOSHIDA, M. NAKANO, Nitrogen and Oxygen Adsorption Properties of Ion-exchanged LSX Zeolite, *KAGAKU KOGAKU RONBUNSHU* 30 (2004) 461–467. <https://doi.org/10.1252/kakoronbunshu.30.461>.
- (16) H. Miyaoka, H. Miyaoka, T. Ichikawa, T. Ichikawa, Y. Kojima, Highly purified hydrogen production from ammonia for PEM fuel cell, *Int J Hydrogen Energy* 43 (2018) 14486–14492. <https://doi.org/10.1016/j.ijhydene.2018.06.065>.
- (17) F. Yoshida, D. Ramaswami, O.A. Hougen, Temperatures and partial pressures at the surfaces of catalyst particles, *AIChE Journal* 8 (1962) 5–11.
- (18) M.M. Dubinin, V.A. Astakhov, Description of adsorption equilibria of vapors on zeolites over wide ranges of temperature and pressure, in: *ACS Publications*, 1971.
- (19) H. Gi, Y. Kashiwara, Y. Itoh, K. Sharma, N. Ogita, H. Miyaoka, T. Ogawa, M. Simanullang, L. Prost, T. Ichikawa, Superdense state of the monolayer hydrogen on adsorbent under liquefied temperature, *Int J Hydrogen Energy* 48 (2023) 3534–3540. <https://doi.org/10.1016/j.ijhydene.2022.10.081>.
- (20) K. Shirono, A. Endo, H. Daiguji, Molecular dynamics study of hydrated faujasite-type zeolites, *J Phys Chem B* 109 (2005) 3446–3453.
- (21) S.Z. Roginsky, Adsorption and Catalysis on Non-Uniform Surface, *USSR Academy* (1949).
- (22) V.P. Zhdanov, A. Krozer, B. Kasemo, Kinetics of first-order phase transitions initiated by diffusion of particles from the surface into the bulk, *Phys Rev B* 47 (1993) 11044.

### Author Introduction



Seiya Kusaka  
Research & Development  
Department



Tomoyuki Ichikawa  
Hydrolabo Inc.



Hiroki Miyaoka  
Hiroshima University



Takayuki Ichikawa  
Hiroshima University

# Research and Development of Ambient-Temperature Hydrogenation Technology for Low-Energy Startup of Ammonia Power Generation

Taro Samukawa, Tomoyuki Ichikawa, Hiroki Miyaoka, Takayuki Ichikawa

## Abstract

Ammonia FC power generation using SOFC (solid oxide fuel cell) is considered to be capable of producing high purity hydrogen and highly efficient power generation because the waste heat from fuel cell power generation can be used to heat ammonia when cracking it to hydrogen. However, it is known that waste heat from fuel cell cannot be utilized during start-up because of the low temperature of the fuel cell, and heating of the reformer by using electric heater is necessary resulting in a large energy loss. Therefore, we conducted research and development of hydrogenation technology at room temperature by the reaction of fluidized ammonia gas and MH (alkali metal hydride) for low-energy startup without using an electric heater.

## 1. Introduction

Currently, as various efforts to combat global warming are being promoted worldwide, countries around the world are working to expand the use of hydrogen as an energy source that does not emit greenhouse gases.

Since hydrogen is in a gaseous state at room temperature, it poses challenges in transportation and storage. As a means of doing so, ammonia has gained attention since it has a high hydrogen density, is easy to liquefy, and excels as a hydrogen carrier.

In ammonia research, in addition to being considered a combustion fuel for engines and gas turbines, extensive studies have been conducted on extracting hydrogen from ammonia for use as a fuel in fuel cells to generate electricity. However, when decomposing (cracking) ammonia into hydrogen and nitrogen, a significant amount of thermal energy is required, including heating the catalyst.

During the startup of a fuel cell power generation system using ammonia, there is no heat source available for ammonia cracking. Therefore, it is necessary to preheat the catalyst using an electric heater or other means. However, this approach has the challenges of requiring a long heating time and consuming a large amount of energy. Alternatively, ammonia combustion could be used as a heat source instead of an electric heater, but this introduces a new issue of NOx emissions (see Figure 1).

As a warm-up method that does not use ammonia, electric heaters, or similar devices, hydrogen combustion using a hydrogen cylinder is available (see Figure 2).

This method allows for easy warm-up by using a hydrogen cylinder. However, a separate hydrogen supply system is required, leading to challenges such as increased system size

Figure 1 Challenges facing power generation systems

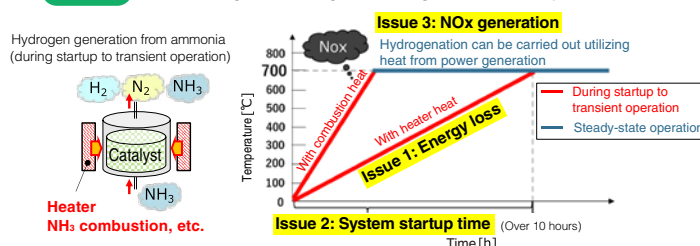


Figure 2 Warm-up method using hydrogen cylinder

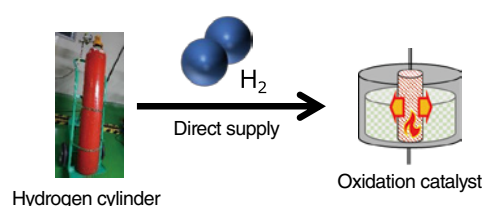
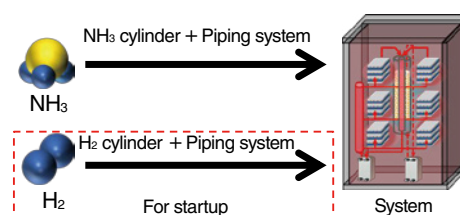


Figure 3 System expansion due to addition of hydrogen supply system



due to the complexity of the power generation system and increased operational complexity due to the need to prepare multiple types of fuel (see Figure 3).

To address the challenge of securing a heat source for warm-up during system startup, we examined the possibility of utilizing the AMMONOLYSIS reaction, which enables hydrogen production from ammonia at room temperature, as a heat source. The AMMONOLYSIS reaction is a technique that generates hydrogen at room temperature through the reaction between ammonia gas and MH. Additionally, since the AMMONOLYSIS reaction is a reversible process, it allows for the regeneration of the MH consumed during system startup (see Figure 4).

If the hydrogen does not contain ammonia, NO<sub>x</sub> will not be generated during combustion, and rapid warm-up can be achieved without consuming power. This enables a clean and low-energy startup in a short time (see Figure 5).

Figure 4 AMMONOLYSIS reaction

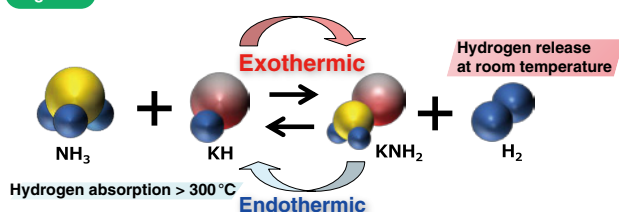
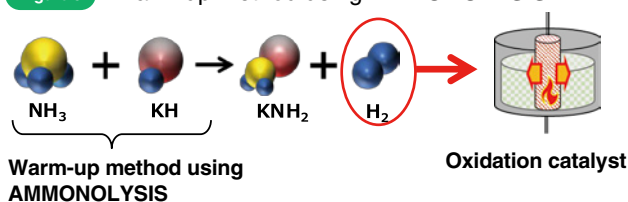


Figure 5 Warm-up method using AMMONOLYSIS



One of the challenges to utilizing the AMMONOLYSIS reaction is the "generation of the amount of hydrogen required for warm-up." Traditionally, research has been conducted on the static AMMONOLYSIS reaction using ambient ammonia gas (Yamamoto et al., 2009). However, for use in warm-up, it is necessary to react flowing ammonia gas with MH to generate the amount of hydrogen required for warm-up.

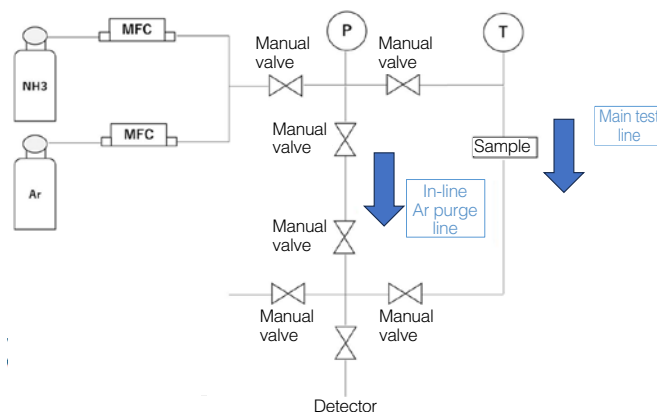
## 2. Evaluation Method

The evaluation of the AMMONOLYSIS reaction using flowing ammonia gas and MH was conducted with the apparatus shown in the diagram below (Figure 6).

First, the characteristics of the apparatus used for evaluating flowing gas are listed below:

- In previous studies evaluating the AMMONOLYSIS reaction using ambient ammonia gas, ammonia gas was supplied to a sealed container containing the sample and then sealed. However, since it was not possible to continuously supply flowing ammonia gas, an apparatus like the one shown in Figure 6 was constructed.
- A purge line was installed to remove residual gas in the piping.

Figure 6 System diagram of flowing gas evaluation apparatus



- A detector was used to analyze the reaction gas after passing through the sample, allowing for the monitoring of hydrogen generation.

The experimental flow is outlined below.

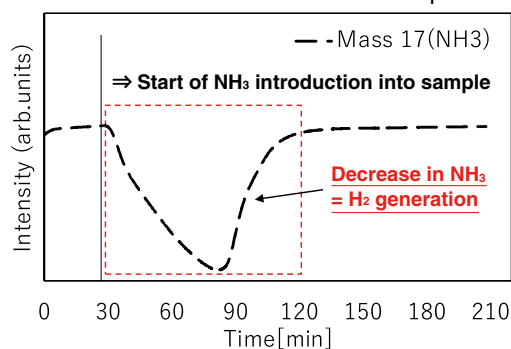
### <Experimental Flow>

- (1) Fill the test container with the measured sample inside a glove box filled with high-purity argon (Ar).
- (2) Install the test container into the testing apparatus.
- (3) To remove residual gas from the piping, switch the valve to the Ar purge line and perform purging.
- (4) Switch the valve to the main test line and supply ammonia gas to the sample, controlling it with a mass flow controller (MFC).
- (5) Analyze the outgoing gas that has passed through the sample using a detector and monitor the amount of hydrogen (H<sub>2</sub>) generated.
- (6) After the test, remove the residual ammonia gas in the piping through Ar purging, close the valves before and after the container, and detach the test container from the apparatus.
- (7) Place the test container back into the glove box filled with Ar gas.
- (8) Remove the sample from the test container and measure its weight.  
By subtracting the pre-test sample weight from the post-test sample weight, the weight increase due to the reaction, A (mg), is obtained. Assuming a 100% reaction, the theoretical weight increase due to amidation is defined as B (mg). The reaction rate of the sample (i.e., the progress of the AMMONOLYSIS reaction) is expressed as the percentage ratio of A to B.
- (9) Analyze the post-test sample using X-ray diffraction (XRD), which provides information on the components and crystal structure in the solid, to confirm the formation of the amidated compound.

## 3. Results

The evaluation results of the AMMONOLYSIS reaction of potassium hydride (KH) in flowing ammonia gas, conducted using the constructed apparatus, are shown in Figure 7.

**Figure 7** Measurement results of amount of ammonia downstream of sample

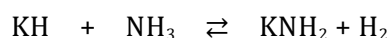


The graph above (Figure 7) shows the results of measuring the ammonia concentration downstream of the sample using the detector inside the apparatus shown in Figure 6.

Compared to the point when ammonia introduction into the sample began (approximately 30 minutes elapsed), the ammonia concentration is observed to decrease between 30 and 120 minutes. From these results, it is evident that the AMMONOLYSIS reaction proceeds even in flowing ammonia gas, consuming ammonia and generating hydrogen.

To confirm the progress of the AMMONOLYSIS reaction, XRD analysis was performed on the samples before and after evaluation. The results are shown in Figures 8 and 9.

The AMMONOLYSIS reaction of KH is represented by the following reaction equation.



Therefore, if the AMMONOLYSIS reaction is progressing, ammonia is consumed, KH is converted into potassium amide ( $\text{KNH}_2$ ), and hydrogen is generated.

The confirmation was actually conducted using XRD. Comparing the XRD measurement results in Figures 8 and 9, it can be observed that the KH peak, which was identifiable before the reaction, has disappeared. Additionally, after the reaction, it was confirmed that  $\text{KNH}_2$  was generated through the AMMONOLYSIS reaction, as indicated by the reaction equation.

Based on the above measurement results, it was confirmed that the AMMONOLYSIS reaction proceeds even in flowing ammonia gas.

**Figure 8** XRD measurement results before evaluation

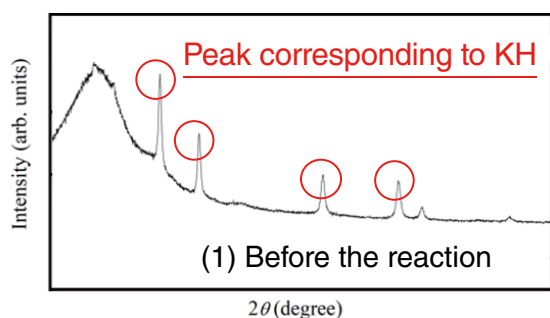
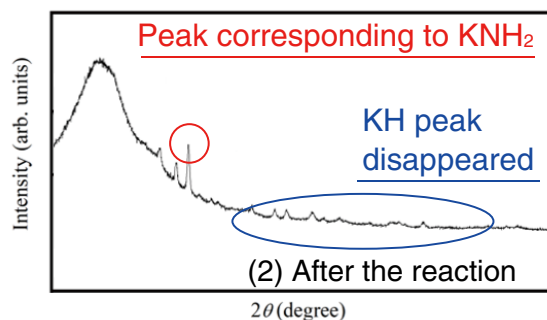


**Figure 9** XRD measurement results after evaluation



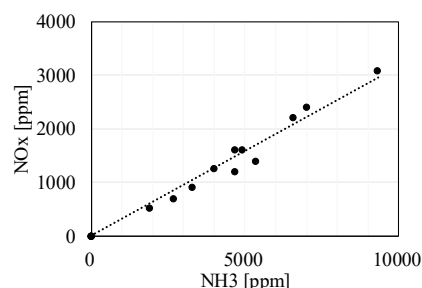
## 4. Challenges and Solutions

From the results of this study, it has been determined that the hydrogen obtained through the AMMONOLYSIS reaction in flowing ammonia gas can be used for warming up the power generation system by combustion.

However, the hydrogen produced through the AMMONOLYSIS reaction in flowing ammonia gas contains a certain amount of residual ammonia. When this residual ammonia-containing hydrogen is combusted, the issue of NOx generation remains.

Figure 10 shows the relationship between the amount of ammonia remaining and the amount of NOx generated.

**Figure 10** Relationship between amount of ammonia remaining and amount of NOx generated



To address this issue, a warm-up system (Figure 11) was constructed that prevents NOx generation by removing ammonia through adsorption after the AMMONOLYSIS reaction.

**Figure 11** Warm-up system under consideration for NOx reduction

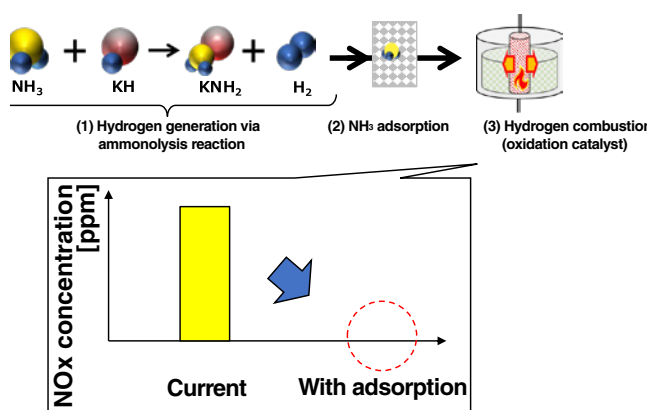
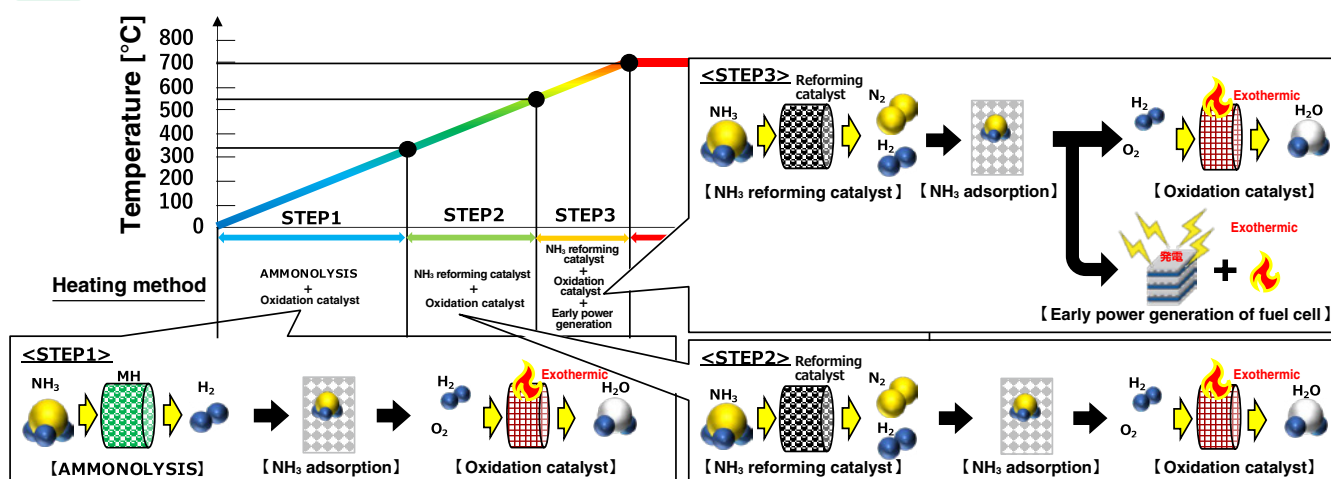


Figure 12 Conceptual image of warm-up system under consideration



In addition, since the alkali metals used in the AMMONOLYSIS reaction pose a high risk, reducing the amount of alkali metal used is also a challenge.

Regarding this challenge, as shown below (Figure 12), it is desirable not to generate all the hydrogen used for warm-up through the AMMONOLYSIS reaction but to switch to the reformer as soon as possible. By changing the hydrogen generation method according to the system temperature, the required amount of alkali metals can be minimized. Below is a system proposal detailing the relationship between system temperature and hydrogen generation methods.

#### <STEP 1>

- Temperature Room temperature to approximately 350°C
- Hydrogen generation method AMMONOLYSIS reaction
- Details At the startup of fuel cell power generation, hydrogen is generated at room temperature using the system shown in Figure 11, followed by combustion. The temperature is increased until the ammonia reformer within the system can operate (approximately 350°C).

#### <STEP 2>

- Temperature 350°C-550°C
- Hydrogen generation method Ammonia reformer
- Details The ammonia supply source has been changed from the AMMONOLYSIS reaction to an ammonia reformer. Ammonia that could not be reformed in the ammonia reformer is removed through adsorption. Warm-up is conducted using hydrogen combustion.

#### <STEP 3>

- Temperature 550°C-700°C
- Hydrogen generation method Ammonia reformer
- Details As in STEP 2, hydrogen is generated using an ammonia reformer. A portion of the hydrogen previously used for combustion is supplied to the fuel cell to initiate power generation at an early stage. Additionally, the heat generated from power generation is utilized to raise the temperature to 700°C.

## 5. Conclusion and Future Outlook

In systems that use ammonia as a fuel, ammonia is difficult to combust at room temperature, so system warm-up is often performed using an alternative fuel such as hydrogen. In contrast, by utilizing the AMMONOLYSIS reaction, we examined the possibility of converting ammonia into hydrogen at room temperature, enabling system warm-up using only ammonia. In this evaluation, it was confirmed that ammonia could be converted into hydrogen via the AMMONOLYSIS reaction even under dynamic gas supply conditions. Additionally, it was found that NO<sub>x</sub> emissions caused by ammonia can be mitigated by incorporating ammonia adsorption.

Moving forward, we will optimize the system utilizing the AMMONOLYSIS reaction, reduce the amount of alkali metal used, and establish safety measures. Furthermore, we will demonstrate the low-temperature startup system currently under consideration and aim to establish a warm-up method that does not require a heater. In addition to FC power generation, we will also explore the technological application of this system for ignition sources in combustors and other uses.

#### Reference:

- (1) H. Yamamoto, H. Miyaoka, S. Hino, H. Nakanishi, T. Ichikawa, Y. Kojima, Recyclable hydrogen storage system composed of ammonia and alkali metal hydride, International Journal of Hydrogen Energy, 34, 9760-9764, 2009.

#### Author Introduction



Taro Samukawa  
Carbon Neutral System  
Development



Takayuki Ichikawa  
Hiroshima University



Hiroki Miyaoka  
Hiroshima University



Tomoyuki Ichikawa  
Hydrolabo Inc.

# Development of the Fuel Tank Closed Valve using a stepping motor

Shinji Murai, Shinji Iwata, Yasuhiro Tsuzuki, Katsuhiko Makino

## Abstract

With tightening of environmental regulations for gasoline evaporation, closed tank systems are expanding for vehicles with small amount of canister purge volume, such as PHEVs. And a pressure control valve is required to shut off the pressure in these tank systems. In this paper, we introduce the compact and lightweight Fuel Tank Closed Valve used a stepping motor.

## 1. Introduction

The regulations on evaporative emissions have been further strengthened to prevent air pollution. The vehicle evaporative emission control system works by temporarily collecting gasoline vapor in a canister, purging the absorbed vapor using the negative pressure from the running engine, and combusting the purged vapor. However, in the automobile market, the number of PHEVs, HEVs, and other environmentally friendly vehicles with excellent fuel economy has been increasing. These types of vehicles have difficulty meeting evaporative emission regulations due to the reduced canister purge volumes.

Recently, a closed fuel tank system has been widely adopted as a technology that allows vehicles with reduced purge volumes to meet regulations. The system requires a control valve to regulate tank pressure. This paper introduces the development of a compact and lightweight fuel tank closed valve using a stepping motor.

## 2. Composition of Closed Fuel Tank System

### 2.1. Comparison between a conventional system and a closed fuel tank system

First, a conventional system is shown in Figure 1. The gasoline vapor generated in the fuel tank is continuously collected in a canister. The collected vapor is then purged using negative pressure in the intake pipe of a running engine and combusted in the engine.

Next, an example of a closed fuel tank system is shown in Figure 2. In this example, a closed valve is positioned between the fuel tank and the canister, allowing gasoline vapor to be absorbed by the canister only when needed. Additionally, a pressure sensor is installed on the fuel tank to continuously monitor its pressure.

Figure 1 Conventional system

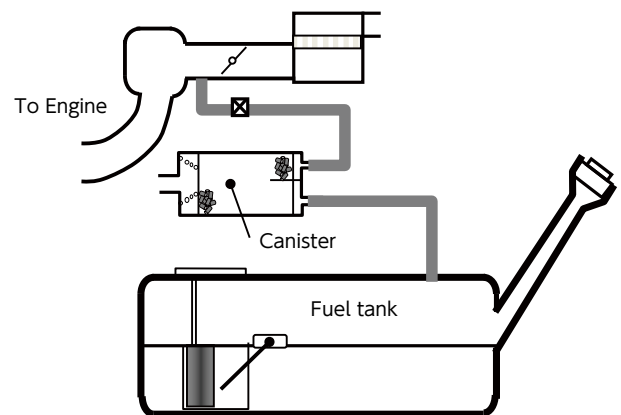
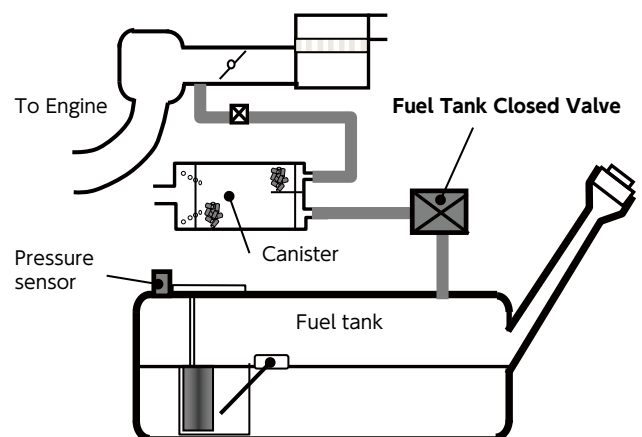


Figure 2 Closed fuel tank system



## 2.2. Functions of the Closed Valve

A closed valve generally needs to fulfill the three main functions shown in (1) to (3) below. Each of these functions is necessary depending on what the vehicle is doing (e.g., when parked, in operation, or being refueled):

- (1) Sealing function (when parked)
- (2) Relief function (when parked)  
(Protection of the fuel tank with a mechanical relief valve)
- (3) Flow rate control function (when in operation and being refueled)

Table 1 shows the required functions based on the situation

**Table 1** Required Functions based on the Situation

Situation	Parking	Driving	Refueling
Required function	(1) Seal function (2) Relief function  Seal up to specified pressure, release pressure if exceeded	(3) Flow control function  Control flow rate according to purge to the purge	(3) Flow control function  Depressurize before refueling, hold fully open to secure flow path

## 3. Development Concept

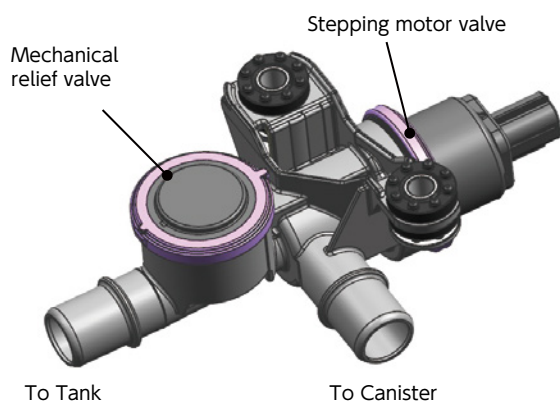
### 3.1. Overview of the Developed Closed Valve

The closed valve was developed to achieve the sealing and flow rate control functions through the integration of the following measures:

- Adoption of a compact stepping motor
- Stroke control using a feed screw mechanism
- Use of a valve with a two-body structure
- Integration of a mechanical relief valve

Figure 3 shows an overview of the developed closed valve.

**Figure 3** Developed Closed Valve



Currently, the solenoid type is the most common type of closed valve that has been commercialized. Table 2 shows a comparison between the closed valve using a stepping motor and a closed valve using a solenoid valve with respect to several specification items.

**Table 2** Comparison with the Solenoid Type

Actuator type	Solenoid	Stepping motor
Refueling	△ Valve opening hold requires energization	○ No energization required for valve open holding
Driving	△ Flow control by on-off Must be responsive	○ Flow control by stroke
Response	○	△
Leakage	○	○
Size	△	○
Weight	×	○

The solenoid type excels in responsiveness but tends to have a larger body structure and be heavier to secure a passage for refueling. In contrast, the stepping motor is less responsive than the solenoid type but is capable of stroke control using a feed screw mechanism, which allows the valve to be downsized.

**Figure 4** Overview of the Stepping Motor

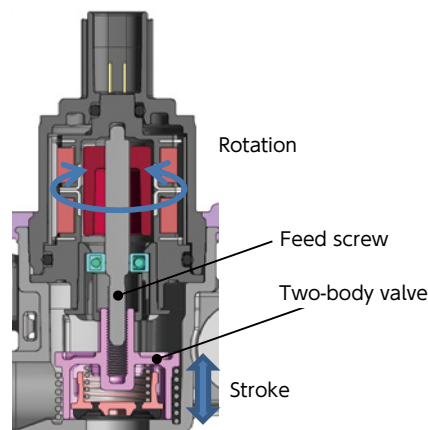


Figure 4 shows an overview of the stepping motor. It can reduce pressure loss when the valve is fully opened for refueling by ensuring a certain stroke amount. Additionally, it can achieve micro flow rate control by reducing the pitch size of the feed screw. Furthermore, reducing the lead angle of the feed screw enables the valve to hold its position against an axial load without energization, thereby reducing power consumption during refueling. Figure 5 shows the relation between friction and lead angles.

**Figure 5** Relation Between Friction Angle and Lead Angle

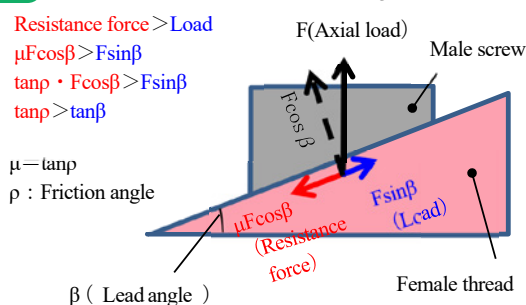
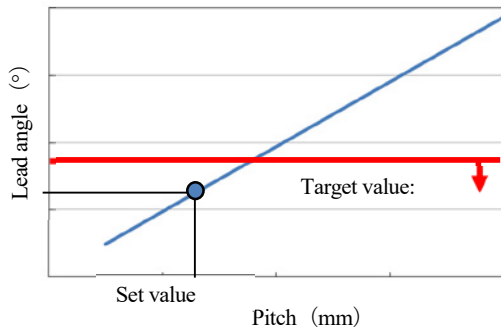


Figure 5 Relation Between Friction Angle and Lead Angle



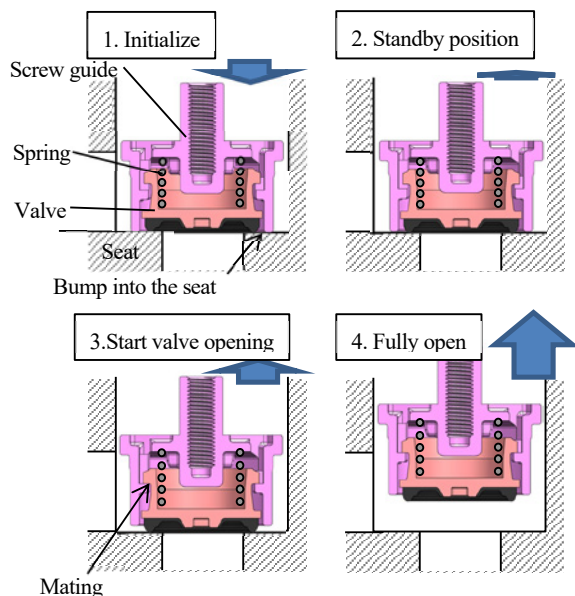
### 3.2. Valve Structure

The stepping motor is characterized by its ability to control its position based on the number of steps from a control origin, without requiring a sensor to detect the position. Therefore, the stepping motor requires initialization to define the control origin.

Initialization is performed with the valve in contact with the seat, which requires the valve to have a rubber member to achieve the sealing function. This raises a concern that variations in the deformation of the rubber due to fluctuations in motor thrust may prevent the sealing function from being stably maintained. Thus, a valve with a spring-loaded, two-body structure has been adopted to achieve both accurate initialization and a reliable seal.

Figure 6 shows the valve structure. This structure enables the initialization to be stably performed with the edge face of a feed screw guide in contact with the seat. This structure allows the valve to be stored inside the screw guide along with a spring, so that the spring force continuously maintains a stable seal. Both the screw guide and the valve have stops that fit into each other, causing the valve to be separated from the seat by a certain stroke.

Figure 6 Valve Structure

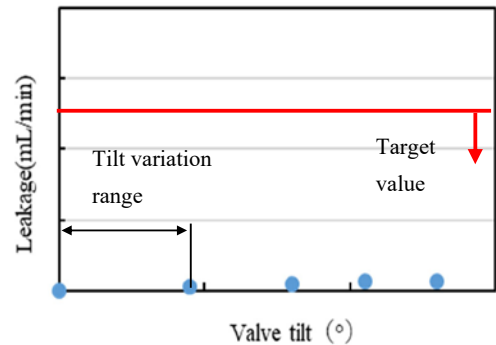


## 4. Performance of the Developed Closed Valve

### 4.1. Sealing Performance

The two-body valve structure provides stable sealing performance. This structure allows the valve to remain aligned with the seat, even when the motor and seat are inclined relative to each other. Figure 7 shows the relation between valve inclination and sealing performance.

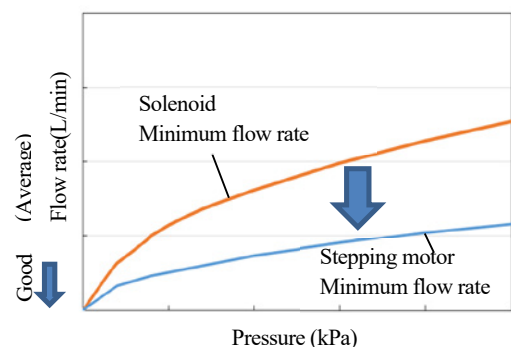
Figure 7 Relation Between Valve Inclination and Sealing Performance



### 4.2. Micro Flow Rate Control

The developed closed valve uses stroke control, achieved through a combination of a motor and a feed screw, to regulate the micro flow rate. As a result, the stroke control enables a vehicle to release pressure even in a state with minute purge amounts. Figure 8 shows a comparison of flow rate characteristics between a solenoid type and a stepping motor type. The stepping motor type is superior to the solenoid type in terms of micro flow rate control, as the solenoid type requires high responsiveness while maintaining sufficient stroke.

Figure 8 Comparison of Flow Rate Characteristics

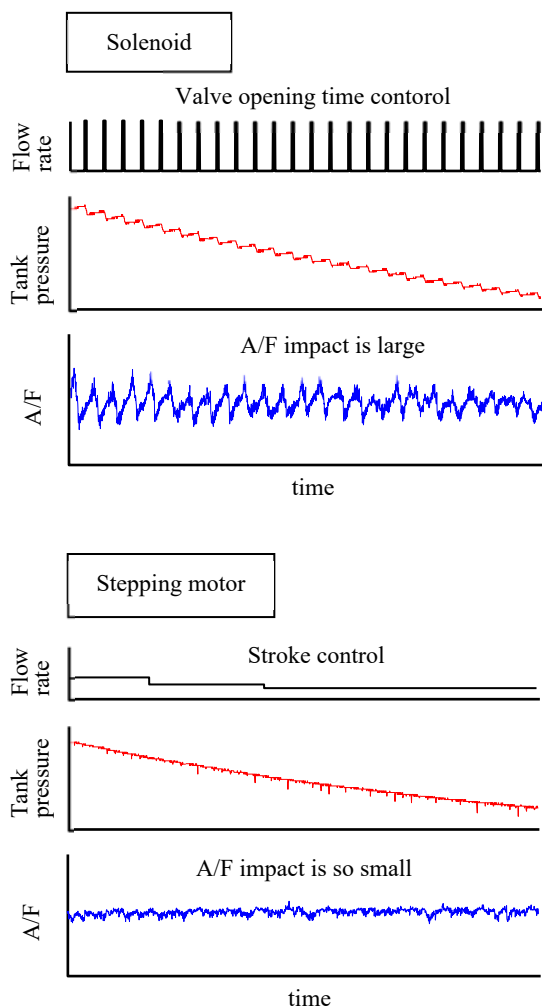


### 4.2. A/F Fluctuation Control

An example of flow rate control while a vehicle is running is the release of pressure from the fuel tank in coordination with purging during engine operation. The solenoid type releases pressure by controlling the valve opening time, which requires a large intermittent flow. This may cause a delay in fuel feedback control, leading to significant A/F fluctuations. In contrast, the stepping motor type releases pressure by controlling the stroke with a small, continuous flow. This allows fuel feedback control

to respond to changes in flow rates and helps suppress A/F fluctuations. As a result, the stepping motor type is expected to improve drivability. Figure 9 illustrates the difference in A/F fluctuations based on the control methods.

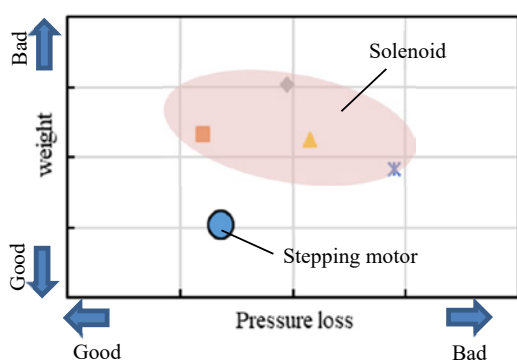
**Figure 9** Difference in A/F Fluctuations based on Control Methods



#### 4.3. Achieving Both Low Pressure Loss and Downsizing

Low pressure loss can be achieved by securing the valve stroke. Downsizing can be achieved by adopting a stepping motor, which is over 40% lighter than the conventional solenoid type, contributing to making it the world's lightest closed valve. Figure 10 shows the pressure losses and weights of the two types.

**Figure 10** Pressure Losses and Weights



## 5. Conclusion

A compact and lightweight fuel tank closed valve was successfully developed by using a stepping motor.

- (1) A closed valve with a two-body structure was developed to ensure both reliable initialization of the stepping motor and stable sealing performance.
- (2) Micro flow rate control based on stroke control contributes to achieving both low pressure loss and downsizing.

Lastly, we express our profound gratitude to all the individuals who supported and cooperated in the development of the fuel tank closed valve.

#### Reference:

- (1) Masanobu Shinagawa, et al., Development of Sealing Valve for Fuel Vapor-containment System, 2006 JSAE Annual Congress (Spring) 20065285
- (2) Akinari Yasue, et al., Development of DC Motor Type EGR Valve with High Flow Rate and Low Leakage, 2017 JSAE Annual Congress (Spring) 20175336

#### Author Introduction



**Shinji Murai**  
First Product Development  
Department



**Shinji Iwata**  
Technology Management  
Department



**Yasuhiro Tsuzuki**  
First Product Development  
Department



**Katsuhiko Makino**  
Research & Development  
Department

# Change in the Resin Material Used for Canisters

Toshiki Tsuboi, Norihisa Yamamoto, Masamitsu Hayakawa

## Adopting polypropylene with low CO<sub>2</sub> emissions effectively reduces CO<sub>2</sub> emissions

Cars release a lot of hydrocarbons (HC) into the air while driving, parking, and refueling. These exhaust gases are collectively referred to as evaporative emissions, or EVAP. Regulations that limit their emissions have been created in various countries and regions (EURO6 in Europe, LEV-III in the Americas, etc.). The canister is an eco-friendly product that follows these rules. It is installed in the pathway between the fuel tank and the atmosphere. It stops the release of HC into the outside environment by adsorbing gasoline vapors that have vaporized inside the tank onto activated carbon. The canister is mostly made of activated carbon and resin. PA66 (polyamide) has typically been used for this resin.

This initiative aims to further improve environmental

performance by replacing this resin material with PP-GF (glass-reinforced polypropylene), which has a simpler manufacturing process and lower CO<sub>2</sub> emissions.

This material is as strong as or stronger than traditional PA66. Because its deformation (how much it bends when under load) is small, the thickness of the plate has also been reduced.

One anticipated concern was the permeability of gasoline vapors, but we created new testing conditions that mimicked our customers and markets. We also verified that the levels were within the regulation limits and replaced the materials. This has made the product more competitive. It now produces 36% less CO<sub>2</sub> and 9% less mass per unit.

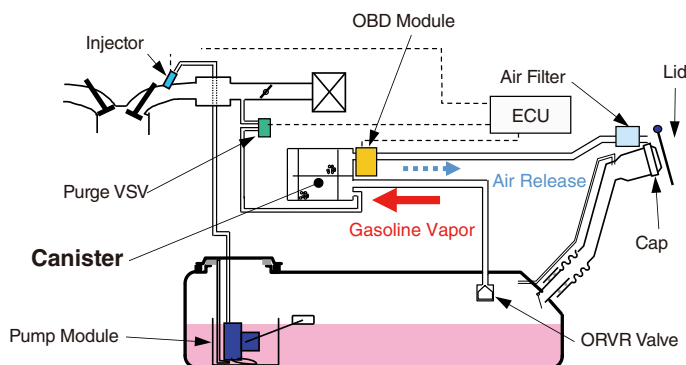
### Highlights of Achievements

## 01

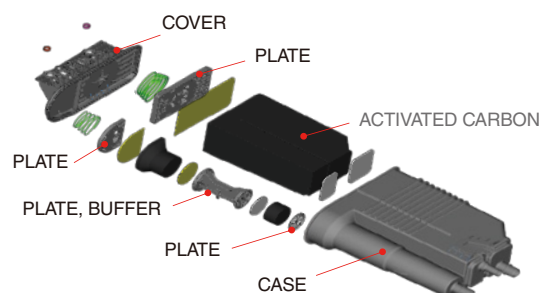
### Use materials that produce less CO<sub>2</sub>

We replaced the resin material of the canister in the fuel tank system (see the figure below) from PA66 (polyamide) to PP-GF (glass-reinforced polypropylene), which greatly reduced CO<sub>2</sub> emissions and mass.

#### 〈 Fuel tank system (ORVR) 〉



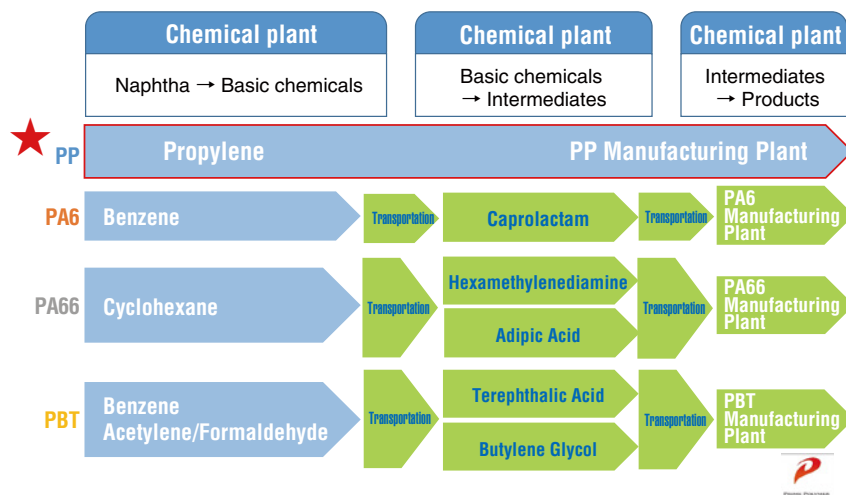
#### 〈 Resin replacement parts 〉



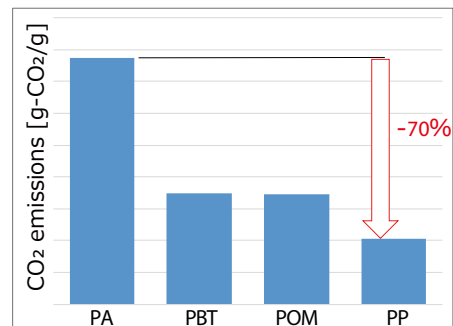
## 02

## Characteristics of alternative materials

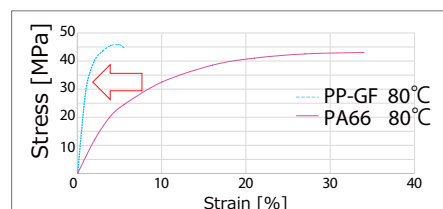
PP-GF (glass-reinforced polypropylene) has a simpler manufacturing process than conventional PA66 and other materials. It also offers advantages in terms of CO<sub>2</sub> emissions per material.



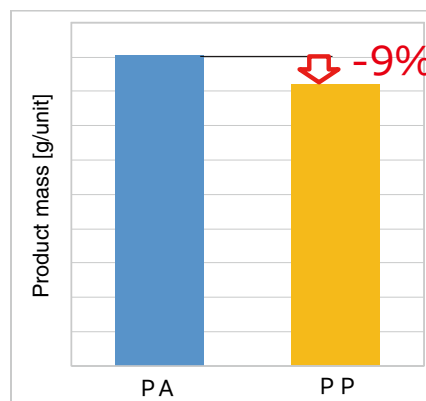
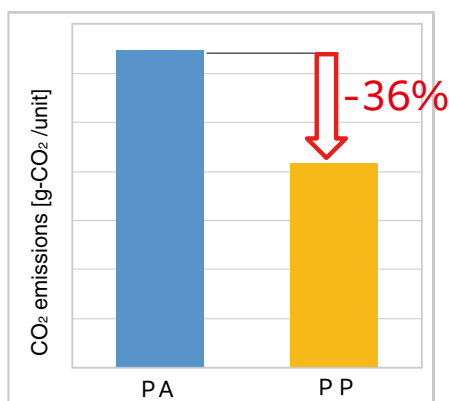
◇ The data listed in this document are representative examples of measurements obtained under specific conditions.  
 Provided by Prime Polymer Co., Ltd.

CO<sub>2</sub> emissions by resin material

## Strength properties comparison

Results  
(Problem Solving)

■ Significant reduction in CO<sub>2</sub> emissions and mass achieved.



## Achievements

- Domestic phase-in: Scheduled to begin in April 2025 with a gradual transition.
- Scheduled to expand to North America and China in the future.



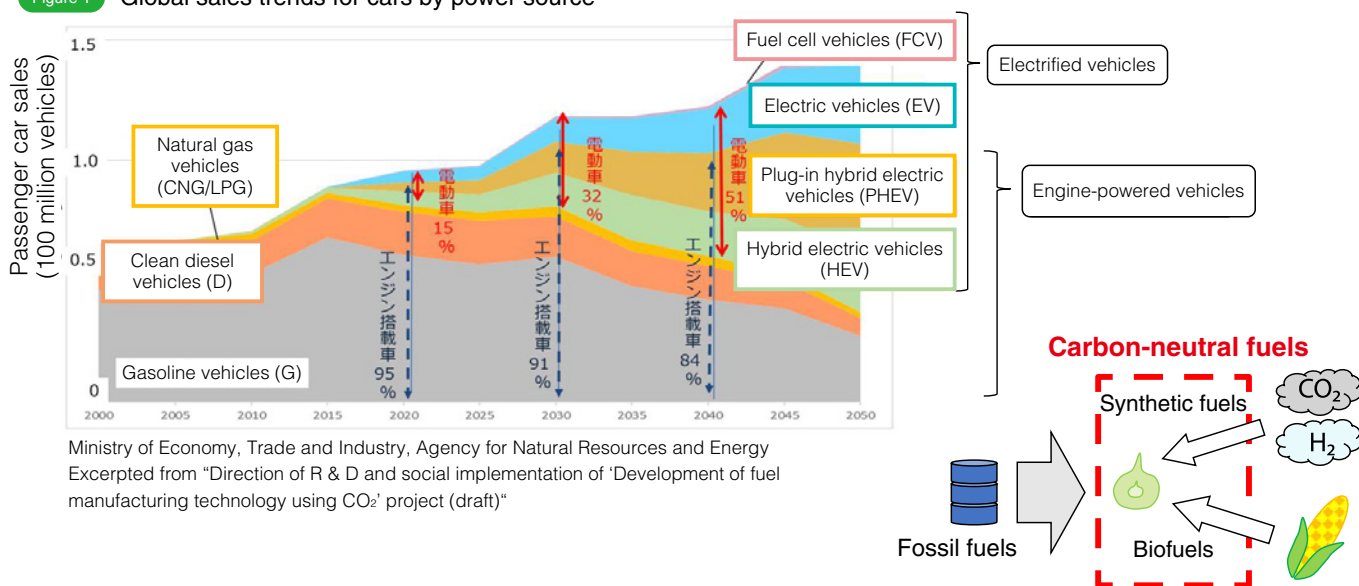
## Electric Pump That Works with Carbon Neutral Fuels

### 1. Overview of the Invention

As shown in Figure 1, the electrification of cars is progressing towards a carbon-neutral society in 2050. Even for engine-powered vehicles, it is expected that there will be a shift toward carbon-neutral fuels, such as synthetic fuels produced by synthesizing CO<sub>2</sub> (carbon dioxide) and H<sub>2</sub> (hydrogen)

from fossil fuels, and biofuels that utilize the energy of living organisms. Hybrid electric vehicles (HEV) and plug-in hybrid electric vehicles (PHEV) are expected to account for a large portion of the market.

Figure 1 Global sales trends for cars by power source

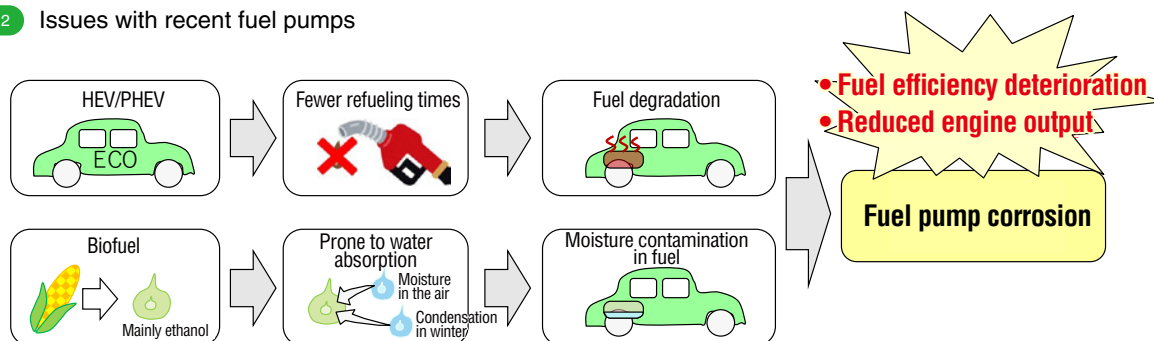


In engine-powered vehicles, including HEV and PHEV, fuel pumps are installed to pump fuel from the tank to the engine. As HEV/PHEV and carbon-neutral fuels become more common, fuel pumps need to be able to handle fuel degradation caused by HEV/PHEV, as shown in Figure 2, and

moisture contamination caused by biofuel.

As fuel pump corrosion progresses, the fuel pump motor's efficiency decreases, which may result in insufficient fuel supply to the engine. This can lead to poor fuel efficiency and decreased engine output.

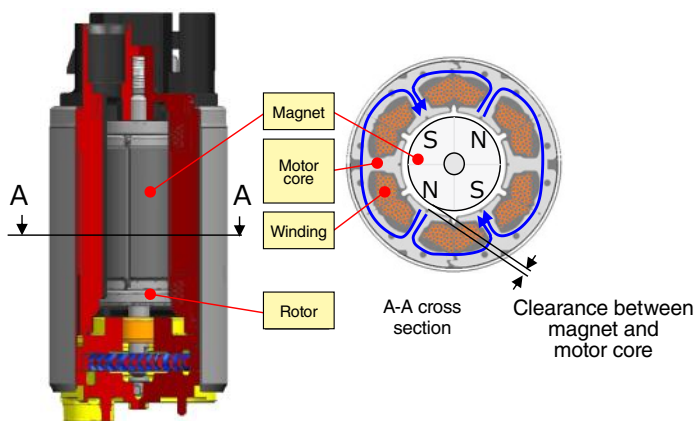
Figure 2 Issues with recent fuel pumps



Brushless motor-type fuel pumps consume less power. The most difficult part of their structure to protect against corrosion is the magnet shown in Figure 3.

Neodymium magnets, commonly used in motors, are susceptible to corrosion because iron is their main component. Figure 4 shows ferrite magnets, which are

Figure 3 Fuel pump cross section



corrosion-resistant. However, they are hard and brittle, making them difficult to attach to the rotor. Additionally, their magnetic force is weaker than neodymium magnets', which significantly decreases motor performance due to the expansion of the clearance between the magnet and the motor core.

Figure 4 Advantages and disadvantages of ferrite magnets

- Main component is iron oxide  
⇒ **Resistant to corrosion** from degraded fuel and water
- ✗ Magnets are hard and brittle  
⇒ **Difficult to fix** to rotating rotors (Adhesives cannot be used because they melt when exposed to fuel)
- ✗ Magnets are weaker than neodymium magnets  
⇒ **Motor performance is significantly reduced due to increased clearance** between magnet and motor core

## 2. Issues with Conventional Inventions and Development Needs

In conventional inventions, such as those represented by Japanese Unexamined Patent Application Publication No. Hei 6-205572, a small-diameter portion is provided in the magnet. A claw for the elastic member joint portion is attached to this small-diameter portion to hold the magnet in place.

However, this configuration has issues described on the right when doing stable fixation under different conditions.

◆ The elastic member is made of soft material: The claws of the joint portion may deform during the assembly process, or there may be insufficient magnet holding force against centrifugal force during motor rotation. → This may cause the magnet to move, requiring an increase in clearance.

◆ The elastic member is made of hard material: Large press-fit allowance of the elastic member. → There is a possibility that the brittle magnet may break during assembly.

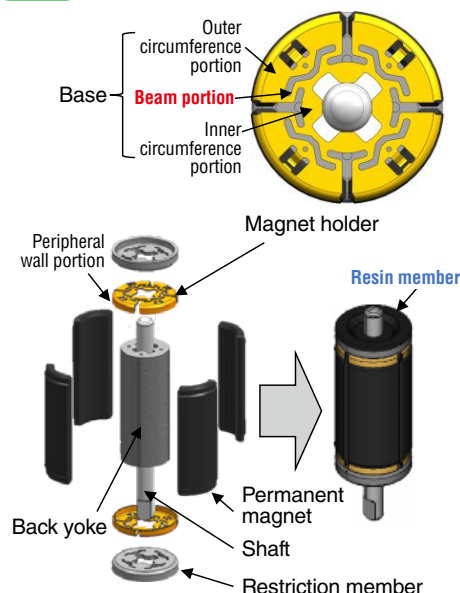
## 3. Features of the Invention, etc.

The present invention solves the problems of conventional inventions by fixing magnets to the rotor using the method shown in Figure 5.

Configuration (a): Deform the beam portion of the magnet holder and hold the permanent magnet in place with radial biasing force

Configuration (b): Seal the through hole with a resin member. Secure the magnet holder so that it does not move due to centrifugal force when the rotor rotate

Figure 5 Magnet fixing method



Because ferrite magnets are brittle, we designed the magnet holder with a deformable beam section to make it more elastic. This allows the peripheral wall portion to hold the magnet in place without applying force during assembly. After assembly, we sealed the beam section with a resin member in the through hole to prevent further deformation.

The above-mentioned fixing method enables stable assembly even when press-fitting conditions vary during assembly, eliminating the need to increase clearance for corrosion or movement of the magnet.

Consequently, it is possible to achieve high motor efficiency equivalent to that of a motor using neodymium magnets, as well as corrosion resistance of the magnet. (See Figures 6 and 7)

The present invention may generate the following secondary effects:

(1) It eliminates the need for surface treatment and other corrosion prevention measures in fuels containing acidic components or moisture. This reduces the environmental load of waste liquid treatment, etc. (2) It does not use rare earth elements such as neodymium, which are concentrated in specific countries, thereby alleviating supply concerns.

The brushless motor-type fuel pump incorporating the present invention is the world's first fuel pump to comply with standards (without requiring a special surface treatment) for different fuel environments in a carbon-neutral society. Mass production began in 2017, helping to bring about a carbon-neutral society.

Figure 6 Motor efficiency comparison

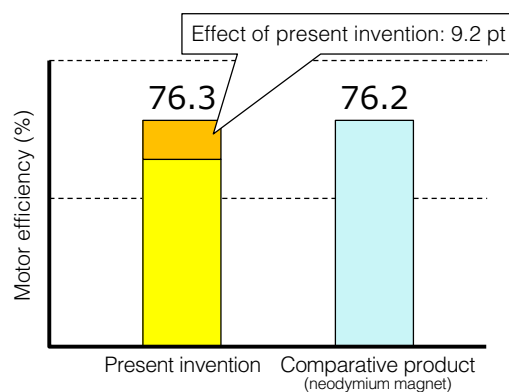






Figure 7 Corrosion comparison results

Present invention		Comparative product (neodymium magnet)	
Ethanol-blended gasoline + water + acid			
Before testing	After testing	Before testing	After testing
			

### Award-Winning Achievements

#### FY2022

Aichi Invention Commendation:

Aichi Invention Award (Aichi Prefecture Invention Association, a General Incorporated Association)

Chubu Region Invention Commendation: Invention

Encouragement Award (Japan Institute of Invention and Innovation, a Public Interest Incorporated Association)

#### FY2024

Chubu Science and Technology Center Commendation:

Promotion Prize (presented by the Public Foundation of Chubu Science and Technology Center, a Public Interest Incorporated Association)



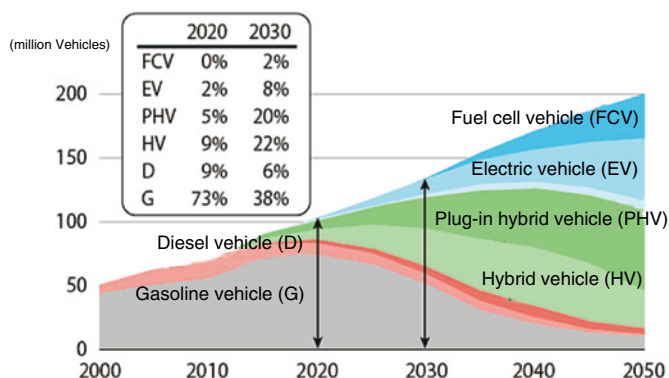


# Air Control Valve for Fuel Cell Systems

## 1. Overview of the Invention

In order to achieve carbon neutrality by 2050, there has been increased attention on hydrogen as a fuel source because it does not emit CO<sub>2</sub> and contributes to energy security by diversifying resource procurement sources. As shown in Figure 1, fuel cell systems that use hydrogen as fuel are expected to become widespread in the form of fuel cell vehicles (FCVs) as well as stationary power generation equipment.

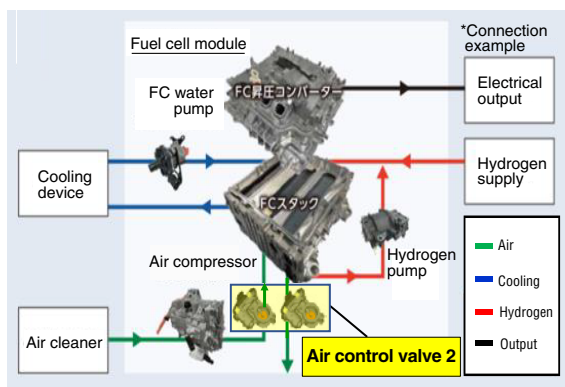
**Figure 1** Forecast of future global vehicle sales by type (Source: SPEEDA Research Institute)



In addition to the hydrogen supply line, fuel cell systems have an air supply line that generates electricity through a chemical reaction with hydrogen. The air supply line is equipped with an "air control valve." (See Figure 2)

The air control valve regulates the airflow rate to achieve the necessary power generation capacity. It also seals the air when power generation stops, preventing a decrease in generating efficiency due to oxidation and deterioration of the fuel cell.

**Figure 2** Fuel cell system diagram (Source: Toyota)



The air control valve requires the following characteristics, so a double eccentric valve type was selected for the configuration. (See Figure 3)

- (1) The opening area is large and capable of handling high flow rates.
- (2) Wear is less likely to occur when the valve body contacts the valve seat when the valve is closed.

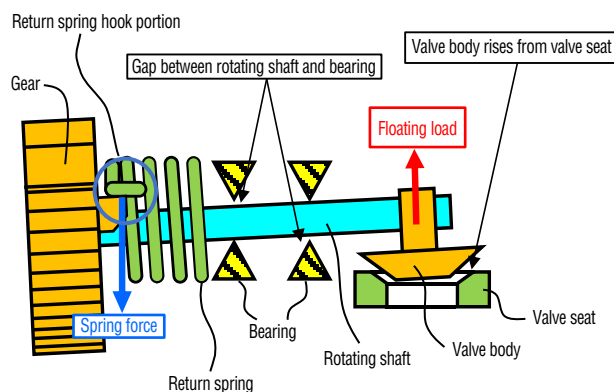
**Figure 3** Comparison of valve configuration characteristics

	Poppet valve	Ball valve	Double eccentric valve
Configuration			
Characteristics			
①	×	○	○
②	○	×	○

## 2. Issues with Conventional Inventions and Development Needs

Although there is a conventional invention for double eccentric valves, as seen in Japanese Unexamined Patent Application Publication No. 2012-72793, when not driven (i.e., when the motor is not energized), the spring force of the return spring causes the rotating shaft to tilt within the gap between the rotating shaft and the bearing. This results in a load, or floating load, that causes the valve body to rise from the valve seat, thereby reducing sealing performance. This necessitates the use of a double eccentric valve capable of maintaining performance when not driven. (See Figure 4)

**Figure 4** Conventional invention issues (schematic diagram)



\*The shape of the parts differs from that of the original invention because this is a schematic diagram.

### 3. Features of the Invention, etc.

The configuration was devised based on the understanding that the floating load when not driven is determined by the relative positions of the "fully closed stopper section" and the "return spring hook section" on the rotating shaft. An xy coordinate system was set up that is perpendicular to the rotating shaft. When this coordinate system is divided into quadrants 1 to 4 for each positive and negative direction of the xy coordinates, the "fully closed stopper section" is positioned in the first quadrant, and the "return spring hook section" is positioned diagonally in the third quadrant. This configuration converts the floating load into a pressing load that presses the valve body against the valve seat, thereby reducing air leakage flow and ensuring sealing functionality. (See Figures 5 and 6)

#### <Features of the present invention>

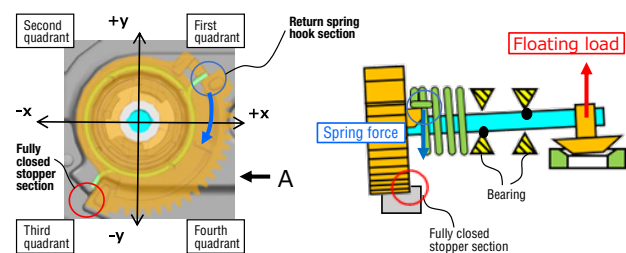
The following unique effects can be obtained without adding any new mechanisms.

- (1) Floating load can be converted into pressing load.
- (2) Pressing load can be maximized.

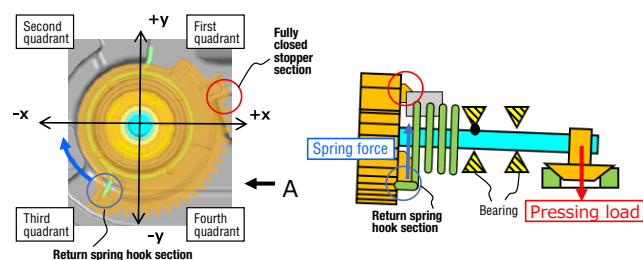
The present invention suppresses the decline in power generation efficiency caused by the oxidation degradation of fuel cells. This is achieved by ensuring the air sealing function of double eccentric valve-type air control valves when power generation stops.

By promoting the widespread use of fuel cell systems equipped with these air control valves, we are helping to establish a carbon-neutral society and reduce CO<sub>2</sub> emissions.

Figure 5 Behavior when not driven

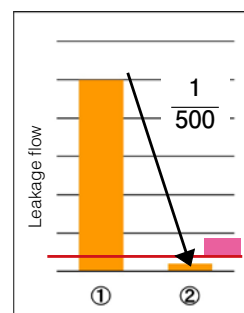


(1) Conventional movement: Behavior when the motor is not powered (floating force generated)



(2) Movement of the invented technology: Behavior when the motor is not powered (pressing force generated)

Figure 6 Comparison of leakage flow



#### Award-Winning Achievements

##### FY2024

Aichi Invention Commendation: Aichi Invention Award (Aichi Prefecture Invention Association, a General Incorporated Association)

Chubu Region Invention Commendation: Invention Encouragement Award (Japan Institute of Invention and Innovation, a Public Interest Incorporated Association)



# Proposal of Phase Shedding Control System for Multiphase PFC Converter

Tatsuya Sakamoto, Hideki Uchiki, Taichi Kawakami

## Abstract

As electric vehicles become more widespread, battery chargers are also becoming more common. A battery charger requires wide-range and high-efficiency operation, which can be achieved by using multi-phase power converters and dynamic phase shedding control. During phase shedding, the state of the power supply undergoes a significant transition, resulting in transient operation. In this technical report, we proposed a new control method that estimates the amount of state transition before and after the phase shedding, thus suppressing transient operation. The validity was confirmed through circuit simulation and verification with actual equipment.

## 1. Introduction

In recent years, the transition to electric vehicles (EVs) has been accelerating as part of efforts to achieve carbon neutrality. Alongside this shift, battery charging has garnered significant attention, leading to an increasing demand for power factor correction (PFC) converters—AC-DC converters designed to improve power factor during charging.

PFC converters are required to support a wide operating range and achieve high efficiency. One approach to achieving this is the multi-phase design of power converters. By implementing a multi-phase configuration, the current flowing through the switching devices can be distributed, thereby reducing conduction losses. As a result, high efficiency can be achieved in the high-output range<sup>(1)</sup>. However, in the low output range, switching losses become more dominant than conduction losses, leading to decreased efficiency as the number of devices increases. Since the optimal phase varies depending on the output range, dynamic phase shedding control is required<sup>(2)</sup>. However, with conventional phase shedding control, the state of the power converter undergoes a significant transition during phase shedding, resulting in fluctuations in the output voltage corresponding to the amount of state transition.

This paper reports on a new phase shedding control method that estimates and suppresses the state transition of the power converter occurring during phase shedding.

## 2. Multi-Phase PFC Converter

### 2.1. PFC Converter

A PFC converter is a device that converts AC power, such as from a commercial power source, into DC current and voltage. During the conversion from AC to DC, if the power factor is low, high-frequency noise caused by distortion and

reactive power are generated. When converting power from AC to DC, a low power factor can lead to the generation of reactive power and high-frequency noise due to distortion. In high-power output power supplies, the effects of distortion increases and may affect other devices become more severe, potentially interfering with the operation of other devices. Since a PFC converter includes a power factor correction function, it can reduce distortion and reactive power. Since a PFC converter includes a power factor correction function, it can resolve issues related to reactive power and distortion. Additionally, according to IEC 61000-3-2 regulations, devices such as AC adapters with an output of 75 W or more are required to incorporate a PFC converter, further increasing the demand for PFC converter circuits.

There are various circuit configuration topologies for PFC converters. In this case, a bridgeless totem-pole PFC converter was selected due to its potential for high efficiency and reduced component count. Figure 1 shows the circuit diagram of the adopted PFC converter. For switches  $S_{1a}$  and  $S_{2a}$ , GaN-HEMTs were used, as these next-generation power semiconductors exhibit low reverse recovery current. By applying PWM control to switches  $S_{1a}$  and  $S_{2a}$ , both the input current and output voltage are regulated. The operating modes of a PFC converter generally include Continuous Conduction Mode (CCM), Boundary Conduction Mode (BCM), and Discontinuous Conduction Mode (DCM). To reduce losses during high-power operation, CCM was selected because it minimizes the peak current flowing through the inductor. A control system, as shown in Figure 2, was designed to regulate the CCM-mode PFC converter. The transfer functions of the PFC converter shown in Figure 2,  $\Delta I_L / \Delta D$  and  $\Delta V_o / \Delta I_L$ , are expressed by the following equations<sup>(3)</sup>:

$$\frac{\Delta I_L}{\Delta D} = \frac{V_{ac}}{R_o(1-D)^3} \times \frac{2 + R_o \times C_o \times s}{\frac{L \times C_o}{(1-D)^2} s^2 + \frac{L}{R_o(1-D)^2} s + 1} \dots (1)$$

$$\frac{\Delta V_o}{\Delta I_L} = \frac{V_{ac} \times R_o}{2 \times V_o} \times \frac{1}{R_o \times C_o \times s + 1} \dots (2)$$

where  $V_{ac}$  represents the root mean square (RMS) value of the input voltage,  $V_o$  represents the RMS value of the output voltage, and  $D$  represents the duty ratio.

From Figure 2, it can be observed that the control system of the PFC converter consists of two major control loops. Among these, the inner loop is responsible for power factor correction control, while the outer loop is for output voltage control. In addition to these loops, disturbances at the frequency of the commercial power supply mains power are always multiplied into the control system after the output voltage compensator. Each loop interferes with the others, and disturbances from the commercial power supply mains frequency also interfere with output voltage control. Therefore, it is necessary to properly design each control compensator to prevent interference between the loops and the disturbances.

Taking these control design methods into account and aiming to accommodate high output, we worked on implementing a multiphase PFC converter.

Figure 3 shows the circuit diagram of the multiphase PFC converter. The validation of the multiphase system was conducted using the simplest two-phase PFC converter. Power factor correction for the first phase is handled by switches  $S_{1b}$  and  $S_{2b}$ , while switches  $S_{3b}$  and  $S_{4b}$  manage power factor correction for the second phase. Full-wave rectification is performed using switches  $S_{5b}$  and  $S_{6b}$ . Additionally, a current balance control mechanism has been introduced to ensure that the current flowing through each phase remains uniform.

By implementing a multiphase configuration, the current flowing through each phase can be reduced, which in turn lowers conduction losses. Additionally, through interleaved operation, inductors  $L_1$  and  $L_2$  can be replaced with a coupled inductor, thereby canceling out the DC superimposed magnetic flux and enabling a reduction in the size of the inductor<sup>(4)</sup>.

Figure 1 Circuit diagram of single-phase Totem-pole bridgeless PFC converter

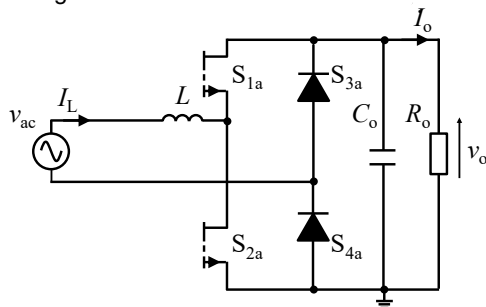


Figure 2 Block diagram of PFC converter

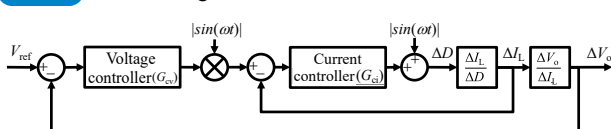
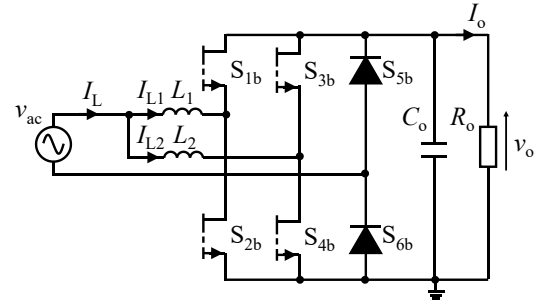


Figure 3 Circuit diagram of multiphase PFC converter



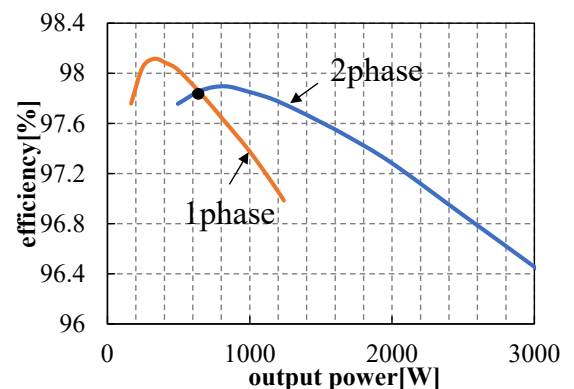
## 2.2. Phase Shedding Control

By adopting a multi-phase configuration, efficiency at high output can be improved. High-efficiency drive operation can be achieved in the high-output range. However, a drawback of this approach is that the number of switching devices increases, leading to greater switching losses. In the low-output range, where switching losses dominate over conduction losses, efficiency deteriorates. Therefore, it is necessary to implement phase shedding according to the output. Therefore, it is necessary to operate with appropriate phase shedding based on the output.

Figure 4 shows the efficiency curve of the PFC converter used in this study. When the output power exceeds approximately 600 W, conduction loss becomes the dominant factor, and the converter operates with higher efficiency in two-phase drive mode. Therefore, phase shedding is necessary around 600 W. However, if the phase shedding threshold is set at exactly 600 W, there is a risk of chattering. To prevent this, the threshold should implement incorporate hysteresis.

Phase shedding allows wide-range and highly efficient operation. However, in conventional control systems, phase shedding induces significant state transitions in the power converter, leading to output voltage fluctuations proportional to the magnitude of the state transition. However, phase shedding in conventional control systems causes a significant transition in the state of the power converter, resulting in output voltage fluctuations corresponding to the amount of state transition. The greater the fluctuation in output voltage, the larger the capacitor with fluctuation suppression functionality needs to be, which is a disadvantage. Therefore, it is necessary to minimize fluctuations in the output voltage corresponding to the amount

Figure 4 Efficiency curves of PFC converter measured at each phase



of state transition as much as possible. In DC-DC converters, control methods for improving this issue have been proposed<sup>(5)</sup>. Since the response speed of output voltage control in PFC converters must be designed to be lower than the mains frequency of commercial power supplies, fluctuations in output voltage become more significant pronounced compared to DC-DC converters. However, this issue has not been investigated.

### 3. Proposed Phase Shedding Control

In this study, a new control system and operational flow were developed to suppress fluctuations during the phase shedding in the PFC converter. Figure 5 illustrates shows the new control system, while Figure 6 presents the operational flow of the control. For phase shedding, the output power of the PFC converter is first checked. At this time, the output power is obtained by multiplying the respective sensor values from the output voltage sensor and the output current sensor installed in the circuit. If the calculated output power value exceeds the shedding threshold,  $S_1$  is toggled. Then, the state transition quantity of the power converter is calculated. The amount of state transition is determined from the deviation between the current value output from each phase before phase shedding  $I_{o \text{ phase before}}$  and the current value output from each phase after phase shedding  $I_{o \text{ phase after}}$ .  $I_{o \text{ phase before}}$  and  $I_{o \text{ phase after}}$  are calculated using the following equation.

$$I_{o \text{ phase before}} = \frac{I_{o \text{ before}}}{N_{\text{before}}} \dots \quad (3)$$

$$I_{o \text{ phase after}} = \frac{I_{o \text{ after}}}{N_{\text{after}}} \dots \quad (4)$$

$I_{o \text{ before}}$  and  $N_{\text{before}}$  represent the sensor value of the output current and the number of phases before phase shedding, respectively, while  $I_{o \text{ after}}$  and  $N_{\text{after}}$  represent the sensor value of the output current and the number of phases after phase shedding, respectively.

The reason for using the current values output from each phase to estimate the amount of state transition was to accurately capture the difference in states before and after phase shedding. In a multi-phase system, each phase is connected in parallel, making it difficult to estimate the amount of state transition before and after phase shedding using either the input voltage or output voltage. In the case of input current, it oscillates at the frequency of the commercial power supply. When sensing the states before and after the shedding, only the instantaneous values of the current can be sensed. The input current value sensed at the timing of the shedding changes. Additionally, if the transition occurs at the zero-crossing point, the amount of state transition becomes extremely small, potentially leading to incorrect sensing. Therefore, it is difficult to use the input current to estimate the amount of state transition. When using the output current flowing through each phase, estimation can be performed using Equations (3) and (4), allowing for the estimation of the amount of state transition while considering both changes in output power and changes in the number of phases. Therefore, the current values output from each phase were used to estimate the amount of state transition.

When the calculation of the amount of state transition is complete,  $S_2$  is turned on, and feedforward (hereinafter, FF) control is initiated. If  $S_2$  is turned off at the moment output voltage fluctuation suppression is confirmed, another state transition of the power converter occurs according to the FF value, causing output voltage fluctuations. Therefore, during FF control, the FF value must be gradually reduced to prevent significant output voltage fluctuations. By turning off  $S_2$  when the FF value reaches zero, no state transition occurs, allowing FF control to be stopped while keeping the control system stable.

The validity of the proposed FF control was confirmed through circuit simulation and testing with actual equipment.

Figure 5 Proposed phase shedding control system

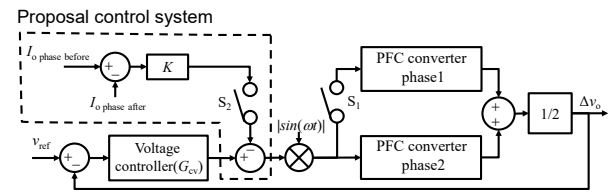
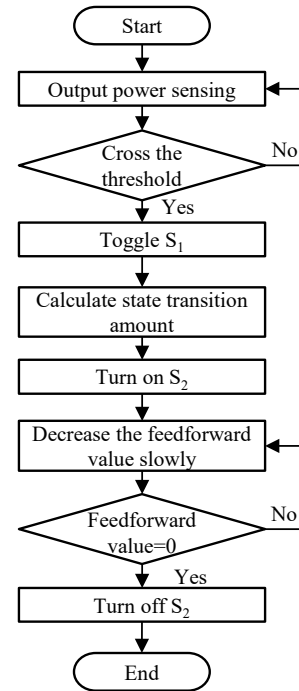


Figure 6 Control flowchart



### 4. Result

A circuit simulator was used to switch the number of phases from one to two during steady-state operation at an output power of 1100 W. Figure 7 shows the results of verifying the effect of FF control in this scenario. With the proposed FF control implemented, the control system operated with a deviation from the target value due to the influence of the FF term. However, when power factor correction control was active, the amplitude of the output voltage fluctuation caused by phase shedding was reduced to approximately one-third.

Next, FF control was implemented in the actual equipment to verify whether similar effects could be achieved with the

**Figure 7** Verification results of ff control using circuit simulator

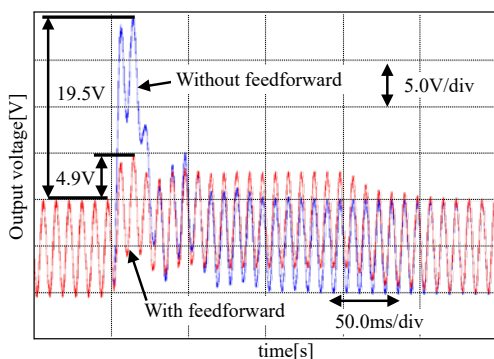


**Figure 8** Measurement results from actual equipment under low load fluctuations

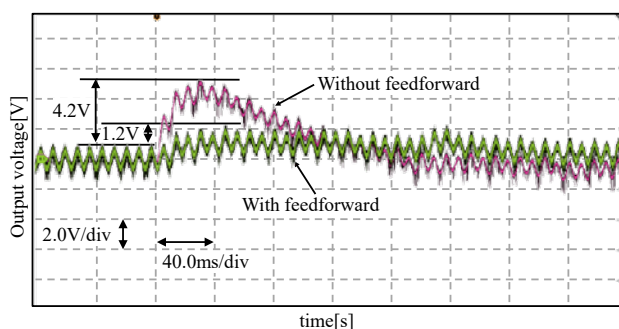
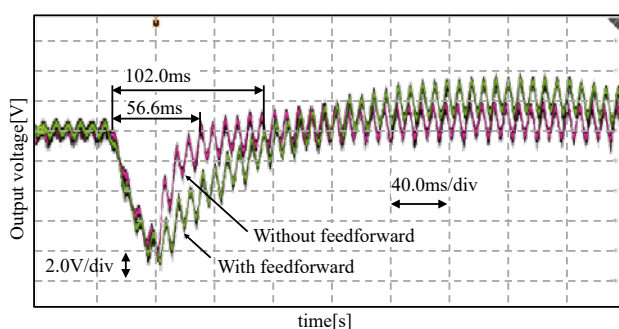


**Figure 9** Measurement results from actual equipment under high load fluctuation



small model. The results of the effectiveness verification on the actual equipment are shown in Figure 8. When the number of phases was changed from one to two during operation at an output power of 40 W, the output voltage was suppressed to approximately one-third by FF control, as shown in Figure 8, similar to the simulation results. However, when the output power was varied from 40 W to 80 W and the number of phases was changed from one to two, the time required to track the target value increased, as shown in Figure 9.

This is because the fluctuation that occurred before the feedforward (FF) control was initiated due to the load variation could not be suppressed, and the FF control started while fluctuations were still present. As a result, the time required to track the target values settling time became longer. Therefore, by optimizing the time from load variation to the initiation of FF control, it is expected that output voltage fluctuations can be suppressed in the same manner as under low-load variation conditions.

## 5. Conclusion

In this technical report, we presented the structure and effects of a phase shedding control system for a multiphase PFC converter. By utilizing output current sensor values to estimate the amount of state transition before and after phase shedding, we were able to account for both changes in output power and the number of phases. Based on this estimated state transition, we constructed a feedforward control system, which successfully reduced output voltage fluctuation amplitude to approximately one-third when phase shedding occurred under low-load variation conditions. These results confirm the effectiveness of the proposed method.

### Reference:

- (1) M. Marcinek, M. Holub: Multiphase, synchronous GaN buck converters – efficiency based selection of the number of phases, EPE'18 ECCE Europe, pp3-7 (2018)
- (2) P. Zumel, C. Fernández: Efficiency improvement in multiphase converter by changing dynamically the number of phases, 37th IEEE Power Electronics Specialists Conference, pp1-6 (2006)
- (3) G. E. Mejía-Ruiz, N. Muñoz-Galeano: Modeling and development of a bridgeless PFC Boost rectifier, Revista Facultad de Ingeniería Universidad de Antioquia, Vol.82, pp9-21 (2017)
- (4) J.Imaoka: Characteristic Analysis and Design of Boost Chopper Circuit using Coupled Inductor for Electric Vehicle, Journal of the Japan Institute of Power Electronics, Vol.39, pp.55-64 (2013)
- (5) A. Costabeber: Digital Time-Optimal Phase Shedding in Multiphase Buck Converters, IEEE Transactions on Power Electronics, Vol.25, pp.2242-2247 (2010)

### Author Introduction



**Tatsuya Sakamoto**  
Research & Development  
Department



**Hideki Uchiki**  
Research & Development  
Department



**Taichi Kawakami**  
Osaka Metropolitan University  
College of Technology

# Estimating the gate-source voltage inside the device

Takahiro Nagao, Hideki Uchiki, Kimihiro Nanamori

## Abstract

In recent years, next-generation semiconductors have been gaining attention in power electronics equipment, with GaN being particularly anticipated for the miniaturization of power converters driven by high frequencies. However, the gate withstand voltage of GaN is approximately 6V, and there is a concern that voltage oscillations during switching could lead to dielectric breakdown. This study proposes a method to model the gate voltage oscillations within the device, including parasitic components of the package and wiring, during the device's ON state. Measurements indicated that the gate voltage oscillated beyond the withstand voltage due to the significant influence of source inductance. However, the model suggested that the internal gate oscillations were smaller and within the withstand voltage range.

## 1. Introduction

In recent years, as the effects of climate change have become more pronounced, environmental considerations have been gaining increasing importance. In response, efforts toward carbon neutrality have been accelerating worldwide, and in Japan, the Green Growth Strategy associated with achieving carbon neutrality by 2050 has been announced(1). The advancement of power electronics technology is expected to play a significant role in achieving carbon neutrality, and the widespread adoption of next-generation semiconductors such as SiC and GaN will greatly contribute to the proliferation of power electronics devices and energy conservation(2) (3). These next-generation semiconductors exhibit superior physical properties, such as bandgap and breakdown electric field, compared to conventional Si semiconductors. In particular, GaN semiconductors are known to adopt a high-electron-mobility transistor (HEMT) structure, allowing the use of the two-dimensional electron gas formed at the AlGaIn/GaN interface as a current path(4). This enables a reduction in input capacitance for devices with the same ON resistance, leading to expectations for the miniaturization and efficiency improvement of power converters through high-frequency operation(5).

In a power converter, power control is performed by switching the power device ON and OFF. When in the ON state, it is necessary to sufficiently reduce the on-resistance of the current path to minimize losses. To achieve this, an overdrive is used, in which a voltage large enough to secure the current path is applied between the gate and source. For GaN devices, a voltage of at least 4.5 V is required for overdrive. However, the gate withstand voltage is relatively low at approximately 6 V, resulting in a small margin between the applied voltage and the withstand voltage(6). Consequently, there is little tolerance for the gate-source withstand voltage, raising concerns that voltage surges and subsequent oscillations due to high-speed

switching could easily exceed the withstand voltage and cause device failure. To address this issue, semiconductor manufacturers are working on defining instantaneous gate withstand voltage ratings(7) and developing GaN devices with higher gate withstand voltages(8).

Additionally, the device's chip is packaged in a resin mold for protection against foreign objects, making it impossible to directly measure the voltage between the gate and source. While the voltage at the electrode terminals on the exterior of the package can be measured, it is affected by parasitic components between the chip and the electrode terminals, making it difficult to obtain an accurate voltage reading.

In this study, we propose a method for estimating the voltage oscillation applied to the gate-source capacitance inside a device by modeling the turn-on behavior of the device in a half-bridge circuit, which is commonly used in power converters, taking into account parasitic components in the wiring and within the device package.

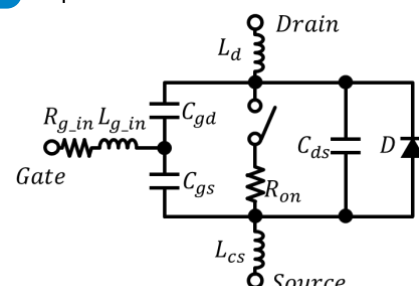
## 2. Circuit Modeling During Turn-On

In this study, we model the switching behavior during the turn-on operation of the Lo side device in a half-bridge circuit.

### 2.1. Parasitic Components of Power Semiconductor Devices

The equivalent model of a GaN device is represented as

Figure 1 Equivalent model of GaN device



shown in Figure 1. In general, the gate voltage refers to the voltage across the gate-source capacitance,  $C_{gs}$ . However, as mentioned earlier, actual measurements inevitably include the effects of factors such as the common source inductance,  $L_{cs}$ , inside the package, as well as the resistance and inductance of the wiring. As a result, accurately measuring the voltage of  $C_{gs}$  is challenging.

## 2.2 Model Construction

Figure 2 illustrates an equivalent circuit of an ideal half-bridge circuit that includes parasitic components of semiconductor devices and the wiring board on which the devices are mounted. To account for the DC current flowing during turn-on, an L-load is connected between the drain and source of the Hi side switch. The DC current is reflected in the model by setting an initial value for the L-load current during calculations. When the Lo side switch turns ON, the Hi side switch is OFF while the Lo side switch is ON. Consequently, the AC current flows through the path via the inter-terminal capacitance on the Hi side, the channel resistance on the Lo side, and the bypass capacitor  $C_{snb}$ . The DC current flows from the power supply through the L load.

**Figure 2** Equivalent circuit that includes parasitic components

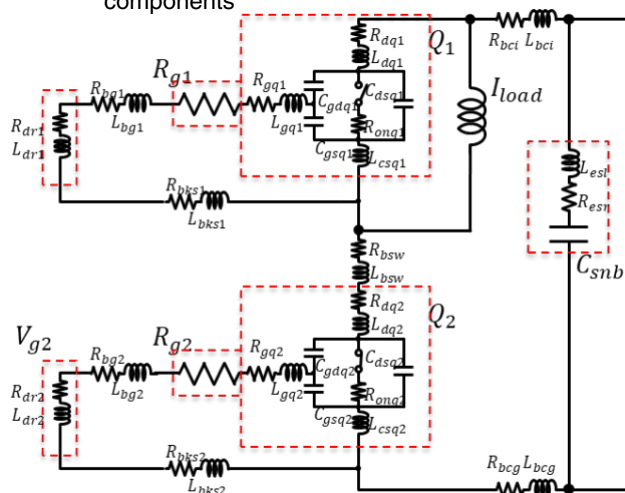
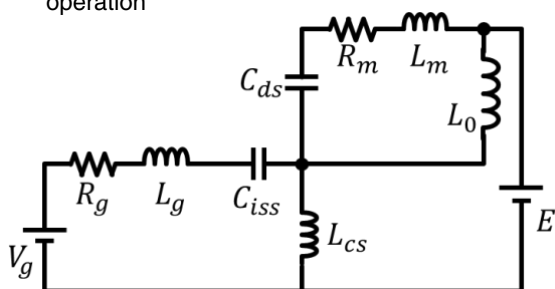


Figure 3 shows a simplified model for representing gate voltage oscillations. Since the Lo side transistor Q2 is in the ON state, its channel resistance is small and can be considered negligible. In this case, the gate-source capacitance  $C_{gs}$  is expressed as the input capacitance  $C_{iss}$ , which includes the feedback capacitance  $C_{gd}$ . In this model, the voltage

**Figure 3** Simplified model of Lo side device during turn-on operation



applied to Ciss is defined as the gate voltage. For the Hi side transistor Q1, when considering the composite capacitance among its drain, source, and gate terminals, the drain-source capacitance Cds is dominant and is therefore reflected in the model. The resistance and inductance components present in the alternating current path are represented as Rm and Lm, respectively. Furthermore, the resistance and inductance components in the Lo side gate drive circuit are denoted as Rg and Lg, respectively, and the voltage applied between the gate and source is represented as Vg. The resistive and inductive components present in the Hi side gate drive circuit do not affect its behavior during turn-on and are therefore omitted in this model.

Since the bypass capacitor  $C_{snb}$  is sufficiently large compared to  $C_{ds}$ , it can be considered a power supply in the AC path. At the same time, it can also serve as the power supply in the DC path, and in this model, it is treated as power supply E.

### 3. Evaluation and Verification

### 3.1. Determination of Parameters and Initial Conditions

To verify the validity of this model, the values of device and Wiring Board parameters were substituted into each parameter of the simplified model to calculate the voltage waveform. Table 1 presents a list of parameters used for the voltage waveform calculation.

The operating conditions were set with a power supply voltage of 100 V and an initial current of 12 A flowing through the inductive load. To simulate switching behavior, at time  $t = 0$ , the model's electrical state was changed by applying step responses to both the power supply voltage  $E$  ( $0 \rightarrow 100$  V) and the Lo side gate voltage  $V_g$  ( $0 \rightarrow 5.2$  V), and the voltage waveform was calculated.

The GaN device used was the EPC2010C. Considering the voltage applied to both the Hi side and Lo side devices immediately before turn-on, the Ciss value was taken from the datasheet at approximately 0 V, while the Cds value was taken at 100 V(7). A common source inductance, Lcs, of 300 pH was used (9). To compare with the actual device data discussed later, the resistance and inductance components of the Wiring Board were analyzed using ANSYS Q3D Extractor based on the Wiring Board design data, and the corresponding parameters were extracted.

Table 1 List of parameters

Symbol	Parameter	Symbol	Parameter
Rm	0.5 $\Omega$	Ciss	420 pF
Lm	7.8 nH	Cds	240 pF
Rg	11.5 $\Omega$	Lcs	300 pH
Lg	19.8 nH	L <sub>0</sub>	174 $\mu$ H
E	0 $\rightarrow$ 100 V	Vg	0 $\rightarrow$ 5.2 V

### 3.2. Verification of Model Validity

To evaluate the validity of the voltage oscillation model, a comparative assessment with actual equipment was conducted using double-pulse evaluation. To measure the gate voltage, a probing terminal was placed as close to the device as possible, and an optically isolated probe (TIVP05, manufactured by Tektronix) was used. A comparison between the measured waveform and the modeled waveform is shown in Figure 4. The dashed line represents the measured waveform, while the solid line represents the modeled waveform. In the comparison waveform shown in Figure 4, the time when the turn-on begins and current starts flowing through the Lo side channel is set as 0 seconds. In this model, transient changes in the device have not been considered, so the waveforms do not overlap. However, the waveform shapes and oscillation frequencies match with high accuracy. Specifically, the oscillation frequency of the modeled waveform is 114.9 MHz, while that of the measured waveform is 117.9 MHz, resulting in an error of 2.5 percent.

When comparing the peak values of the gate voltage, the peak value of the modeled waveform was 8.51 V, while the peak value of the measured waveform was 7.42 V, resulting in an error of 12.8 percent. This discrepancy is likely because, in the modeled waveform, E and Vg were given a step response to simulate switching behavior. Consequently, the change was steeper than the measured waveform, leading to the observed difference in the peak gate voltage.

### 3.3. Estimation of Internal Gate Voltage of Device

Using this model, we estimate the actual gate voltage inside the device (Ciss voltage in this model). Figure 5 shows the voltage waveform of Ciss calculated under the same conditions using the model. As seen in Figure 5, the oscillation of the Ciss voltage is smaller than the voltage that includes Lcs, which can actually be measured. The peak voltage is 5.80 V, which falls within the withstand voltage range. This indicates that the reverse electromotive force generated in the inductance due to the change in current during turn-on has a significant effect. The magnitude of the generated reverse electromotive force V is expressed using the change in drain current  $dI_d/dt$  in equation (i).

$$V = L_{cs} * \frac{dI_d}{dt} \dots \dots \dots (i)$$

Although Lcs is as small as 300 pH, the current in GaN changes on the order of several nanoseconds. As a result, the change in drain current is large, leading to a significant induced electromotive force. Consequently, there is likely a considerable discrepancy between the measured voltage waveform and the actual gate voltage inside the device. A significant drop in gate voltage immediately after switching begins is also considered to be influenced by Lcs. The waveform estimated from the model suggests that the peak gate voltage inside the device is lower than the measured value and does not exhibit large voltage oscillations as seen in the measurements. Therefore, even for devices with low

Figure 4 Comparison of measured waveform and modeled waveform

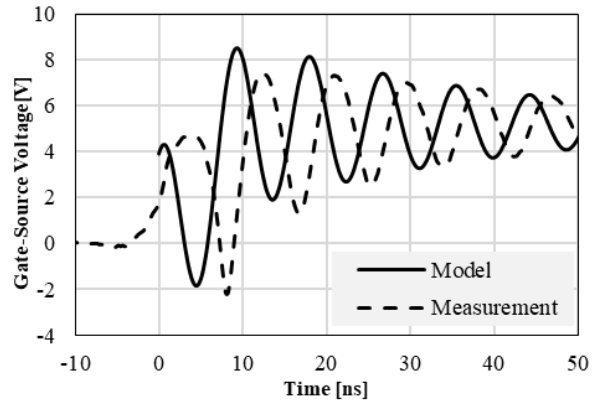


Figure 5 Voltage waveform of internal gate voltage of device calculated using the model

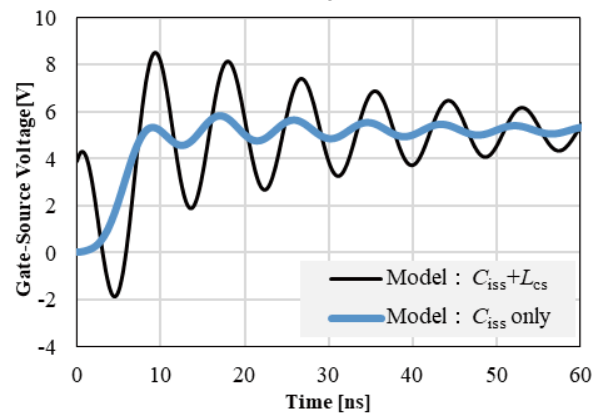
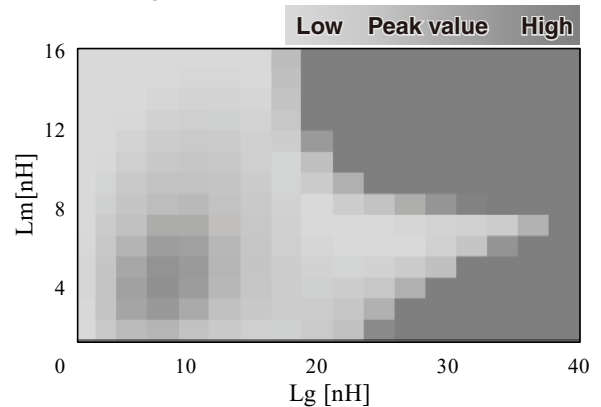


Figure 6 Peak value mapping of gate voltage when Lm and Lg are varied



gate withstand voltage, such as GaN, it can be assumed that they operate without issues. As a result, it becomes possible to further increase the switching speed or apply a higher gate voltage, thereby reducing switching losses.

Figure 6 presents a peak value mapping of the gate voltage when the two inductances, Lm and Lg, in the model are varied parametrically. In general, inductance in switching circuits is required to be minimized. However, as shown in Figure 6, simply reducing the inductance does not necessarily minimize the peak value. By designing the two values in a well-balanced manner, it becomes possible to suppress the peak value of gate voltage oscillation during turn-on.

## 4. Conclusion

In this study, a circuit model for the turn-on operation of a half-bridge circuit, a common switching circuit, was developed by taking into account the parasitic components included in the device package and the Wiring Board. By using this model, we demonstrated a method for estimating the internal behavior of a device that is difficult to measure in practice. When switching with GaN, the gate withstand voltage is low, making it susceptible to dielectric breakdown due to surges at turn-on and subsequent oscillations. With high-speed switching, when there is a significant change in current, the back electromotive force of the common source inductance causes a substantial difference between the measured waveform and the gate voltage inside the device. However, by using this model to estimate the internal gate voltage of the device, it becomes possible to determine whether the voltage exceeds the withstand voltage. This enables the miniaturization and efficiency improvement of power electronics equipment, making full use of GaN's characteristics of high-speed switching and low loss.

### Reference:

- (1) Ministry of Economy, Trade and Industry, et al., Green Growth Strategy Through Achieving Carbon Neutrality in 2050, 6, (2021)
- (2) Yoshikazu Takahashi, Akira Morozumi, Yoshitaka Nishimura, Trends of Power Module Package Technology, Supporting Power Electronics. In Proceedings of the 26th Microelectronics Symposium (pp. 15-22), The Japan Institute of Electronics Packaging (2016)
- (3) IMAOKA, J, The Latest Trend of Power Electronics for Carbon Neutrality and Applied Technologies of Magnetic Components–High Power Density / High Efficiency / Modeling–, Journal of the Japan Society of Applied Electromagnetics and Mechanics, 30(1), (2022)
- (4) Katsuaki Suganuma, Packaging and Reliability Evaluation Technologies for SiC/GaN Power Semiconductors (pp. 54-59) (2014)
- (5) Manabu Yoshino, Yujiro Takeuchi, Kota Ohi, Akira Nakajima, Latest Technology Trends in Power Semiconductor Devices, IEEEJ Transactions on Electronics, Information and Systems, 144(3), (pp.186-192) (2024)
- (6) Efficient Power Conversion Corporation: EPC2010C Datasheet, Revised April 2021
- (7) GaN Systems: GS66516T Datasheet, Rev211025
- (8) ROHM Co., Ltd. website  
[https://www.rohm.co.jp/news-detail?news-title=2022-03-23\\_news\\_gan-hemt&defaultGroupId](https://www.rohm.co.jp/news-detail?news-title=2022-03-23_news_gan-hemt&defaultGroupId)
- (9) David Reusch (Efficient Power Conversion Corporation): White Paper: WP009, (2020)

### Author Introduction



**Takahiro Nagao**  
Research & Development  
Department



**Hideki Uchiki**  
Research & Development  
Department



**Kimihiro Nanamori**  
National Institute of Technology  
(KOSEN), Maizuru College

# Development and Practical Application of ADC12 Aluminum Alloy Semi-Solid Die Casting Mass Production Technology Using Mechanical Vibration

Masayuki Kito, Junichi Shinoda, Ryo Koide, Yuta Ichimura, Yuichiro Murakami, Kenji Miwa

## Abstract

The semi-solid die casting method has advantages such as reduction of casting defects and improvement of dimensional accuracy. On the other hand, ADC12 alloy, which is widely used as a die casting alloy, is difficult to be used for semi-solid die casting because of its narrow temperature range which is suitable for semi-solid slurry formation. In this development, ADC12 alloy slurry was successfully formed by applying mechanical vibration to the cooling process from the molten state to the solid-liquid coexistence temperature and optimizing the conditions. In addition, this technology was realized in the mass production process, and it was adopted for hydrogen supply unit components used in FCEV (Fuel Cell Electric Vehicle).

## 1. Introduction

Amid the growing need for carbon neutrality in the automobile industry, there has been an increased demand for high-quality, lightweight, and cost-effective aluminum raw materials.

Figure 1 Relation between costs and quality

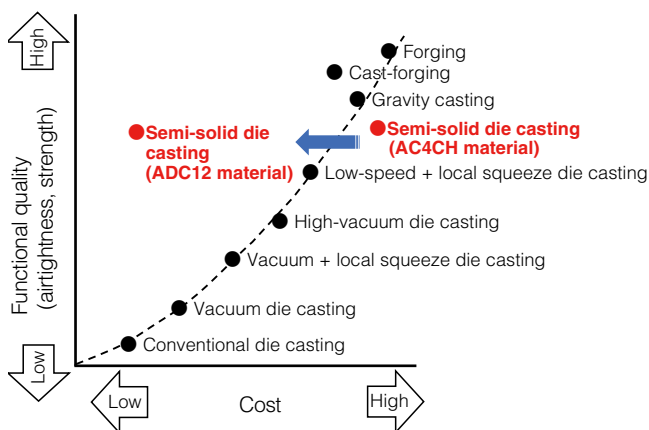


Figure 1 shows a correlation curve between functional quality and costs for a method of producing aluminum raw materials, illustrating a relationship in which an increase in functional quality leads to higher costs.

In conventional semi-solid die casting (DC), AC4CH aluminum alloy materials have generally been used. However, these materials have the following drawbacks that contribute to high costs:

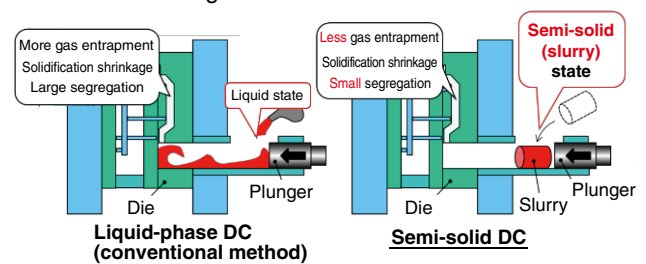
- Low market distribution volume, leading to high material costs;
- Low fluidity, resulting in large wall thicknesses depending on the shape;
- Low mechanical properties, requiring post-processing such as heat treatment based on quality requirements.

Thus, development was carried out to use ADC12 aluminum alloy materials, which have large market distribution and are commonly used in relatively inexpensive die casting, for semi-solid die casting. This approach achieves both high-quality and cost-effective aluminum rough shape materials, ultimately meeting market demands.

## 2. Characteristics of Semi-Solid DC

In general, in liquid-phase die casting, rippling of the liquid traps air, as shown in Figure 2, and the transition from the liquid to solid phases causes the material to shrink.

Figure 2 Differences between liquid-phase and semi-solid die casting



These phenomena cause porosity due to air entrapment and shrinkage, as well as segregation of alloy compositions caused by rapid cooling. These factors reduce internal quality and are inevitable issues associated with high-speed molding of liquid metal.

In contrast, semi-solid die casting uses a slurry in which metal is in a semi-solid state at a temperature lower than that of liquid-phase die casting. Therefore, semi-solid die casting is expected to reduce coagulation shrinkage and porosity, as well as improve dimensional reproducibility.

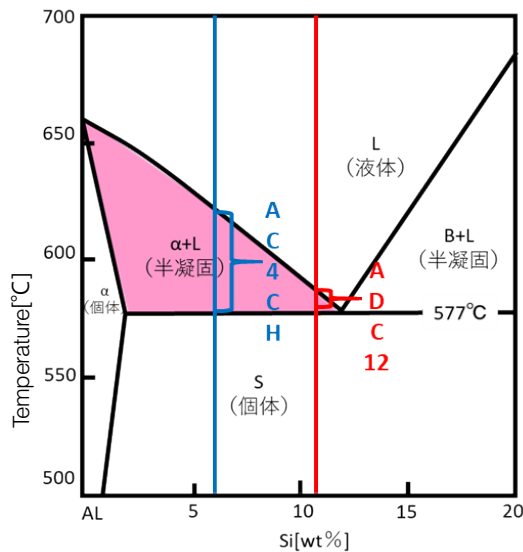
Additionally, semi-solid die casting can help reduce porosity by preventing air entrapment, as there is no rippling during injection when the plunger starts to move.

Furthermore, since the material filling the mold is in a slurry state with a relatively uniform metallographic structure, semi-solid die casting is expected to reduce segregation and fluctuations in mechanical properties, thereby improving the mean values of these parameters.

Therefore, semi-solid die casting is considered a fundamental solution to the problems involved in conventional die casting of liquid metal. However, it also has some disadvantages.

The first disadvantage is the risk of underfill due to the reduced fluidity caused by pouring a high-viscosity fluid into a mold.

Figure 3 AL-Si binary state diagram



The second disadvantage is the challenges associated with the material characteristics of ADC12 when applied to die casting.

As shown in the state diagram in Figure 3, ADC12 has a smaller temperature range where the material can exist in a solid-liquid coexistence state compared to AC4CH. This makes it more difficult to control the temperature and produce a semi-solid metal slurry.

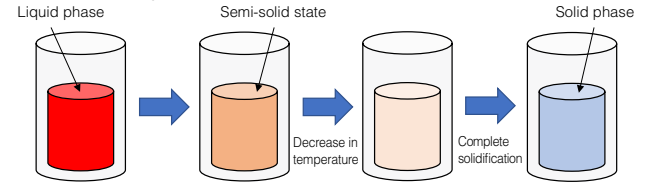
Additionally, as shown in Figure 4, ADC12 and AC4CH exhibit different coagulation patterns. AC4CH coagulates uniformly in a gruel-like state, while ADC12 coagulates from the peripheral sections, where the temperature decreases faster than in other areas. This can lead to an uneven solid phase ratio within the slurry and result in segregation. Therefore, although ADC12 is low in cost and high in strength, it has been considered a material that is difficult to use for producing high-quality semi-solid slurry with a uniform solid phase.

### 3. Producing the Semi-Solid Slurry of ADC12 Alloy

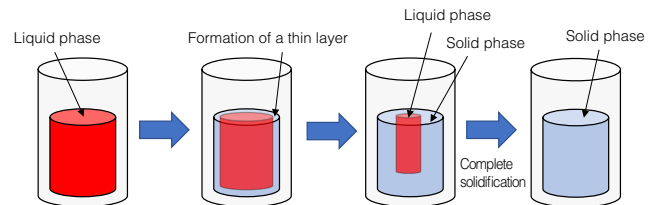
In the production of the ADC12 alloy slurry, molten metal is poured into a container, which is mechanically vibrated at a temperature lower than that of the molten metal. The metal is then cooled while being circulated by convection, reaching a solid-liquid coexistence state.

When molten metal is cooled, a solid phase precipitates on the surface of the container, which is at a lower temperature than that of the molten metal.

Figure 4 Image showing the difference in coagulation by alloy



Slurry-type solidification image (AC4CH alloy)



Skin-formation type solidification image (ADC12 alloy)

Figure 5 Conceptual image of slurry production

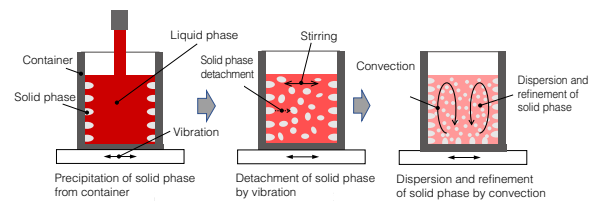
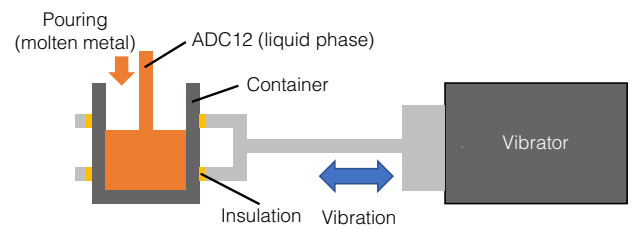


Figure 6 Conceptual image of mechanical vibration device



A conceptual image of this process is shown in Figure 5.

Conventionally, AC4CH slurry has been produced by causing molten metal to flow in a rotational direction, such as with electromagnetic stirring, which disperses and refines the solid phase that precipitates on the surface of the container. However, this method cannot produce a favorable ADC12 slurry, as a hard initial solidifying shell forms on the contact surface between the ADC12 and the container.

Therefore, to obtain a favorable ADC12 slurry, a strong stirring force through mechanical vibration is applied to the molten metal, which separates the solid phase from the surface of the container.

Figure 6 shows a conceptual image of a mechanical vibration device used to produce ADC12 slurry.

The device enhances the dispersion and refinement of the solid phase through convection, thereby equalizing the solid phase. In this way, a method has been established for producing high-quality slurry through the optimal application of mechanical vibration.

Figure 7 shows the effect of the slurry production method using mechanical vibration.

When no vibration was applied, a coarse structure

**Figure 7** Observation of the structure of ADC12 alloy slurry

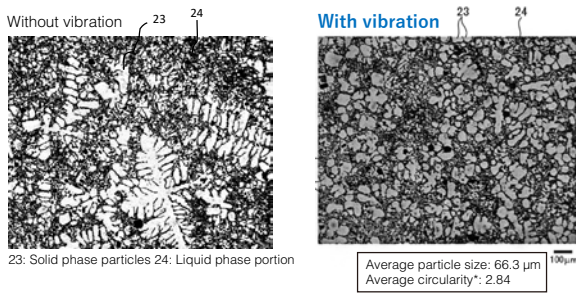
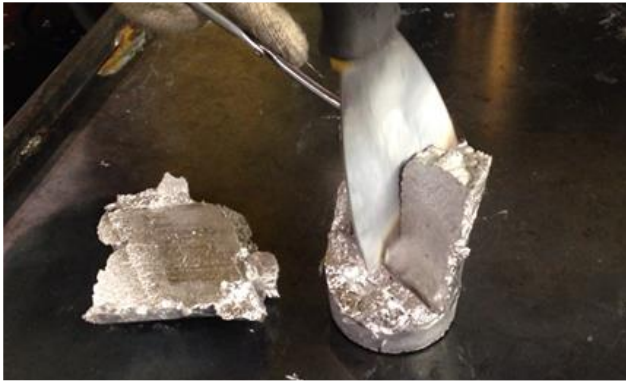


**Figure 8** Observation of cutting ADC12 alloy slurry



growing into a dendrite-like form was observed. In contrast, when vibration was applied, the structure was refined and a favorable semi-solid slurry was obtainable in terms of the smallness of the mean particle size and the mean circularity of solid phase particles, which were considered to be ideal for maintaining the features of raw materials.

Additionally, the method was able to produce a slurry with uniform hardness from its surface to its interior, allowing it to be easily cut with a metal spatula. The cut section was smooth and clean (see Figure 8).

#### 4. Challenges in Maintaining the Fluidity of the Slurry

Using a mold capable of producing a spiral test piece for evaluating flow lengths, the influence of shear stress on flow length was evaluated by varying gate thicknesses and injection speeds.

Using the spiral test piece shown in Figure 9, the relation between gate thickness and flow length was evaluated, as shown in Figure 10.

The flow length of ADC12 in a semi-solid state tends to increase as the gate thickness is reduced.

In the case of a gate thickness of 4.0 mm, the flow length was considered to have increased due to the decrease in flow resistance.

Next, the parameters used in the flow length test were reorganized using the following equations:

$$\text{Shear rate: } \dot{\gamma} = 6Q / (BH^2) = 6V / H$$

(where  $\dot{\gamma}$  is the shear rate,  $V$  is the gate speed,  $Q$  is the volume flow rate,  $B$  is the gate width, and  $H$  is the gate

**Figure 9** Spiral test piece

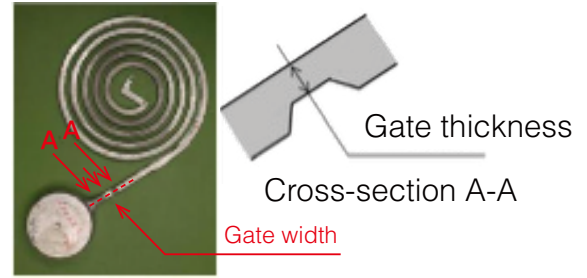
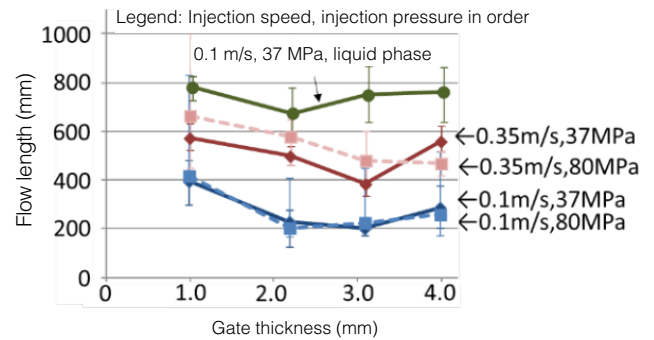


**Figure 10** Relation between gate thickness and flow length



thickness), and

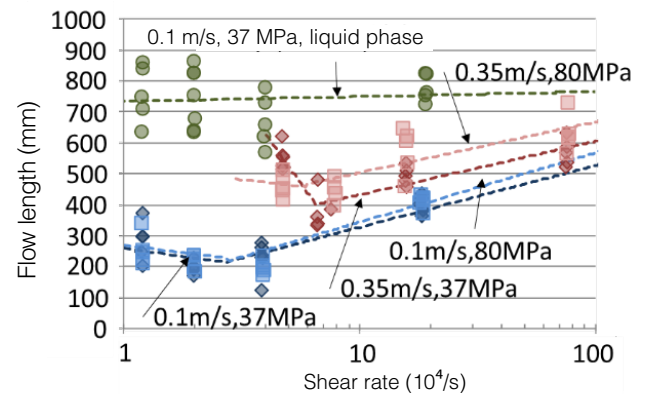
$$\text{Shear stress: } \tau = \dot{\gamma} \cdot \eta$$

where  $\eta$  is the apparent viscosity.

The shear rate increases as the gate width and thickness are reduced. Additionally, the shear rate increases as the gate speed is increased.

Figure 11 shows the reorganized relation between the calculated shear rates and flow lengths.

**Figure 11** Relation between shear rates and flow lengths



In a semi-solid state, the flow length is enhanced when the shear rate is increased above a certain amount. This suggests that the slurry fluidity improves due to the reduction in slurry viscosity when the shear rate at the gate is increased, causing the slurry to experience greater shear stress.

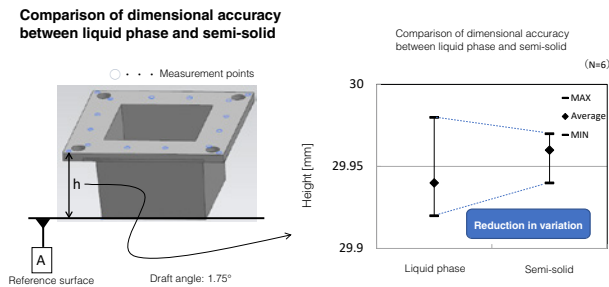
Accordingly, it was confirmed that applying a certain level of shear rate allows a flow length similar to that of the liquid phase to be maintained.

#### 5. Dimensional Accuracy and Mechanical Properties

The influence of phase differences on dimensional accuracy

was evaluated by comparing the products shown in Figure 12, which were produced through liquid-phase and semi-solid die casting.

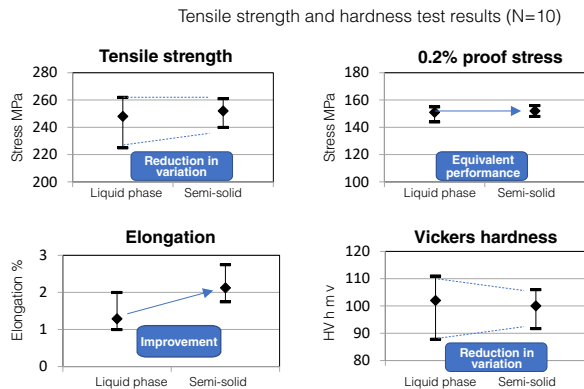
**Figure 12** Comparison of dimensional accuracy between liquid-phase and semi-solid die casting



The product produced through semi-solid die casting exhibited reduced dimensional variation compared to the product produced through liquid-phase die casting. This suggests that the smaller shrinkage rate in semi-solid die casting, compared to liquid-phase die casting, contributed to the improvement in dimensional reproducibility.

Next, mechanical property tests were conducted using test pieces ( $\phi 10$ ) produced through liquid-phase and semi-solid die casting. The results of the comparative evaluation of the mechanical properties are shown in Figure 13.

**Figure 13** Mechanical properties of liquid-phase and semi-solid die casting



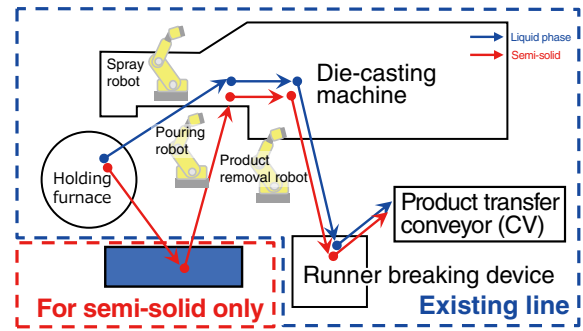
The test piece produced through semi-solid die casting exhibited improved elongation compared to the one produced through liquid-phase die casting, with equivalent properties for the other test parameters. This suggests that the application of vibration contributed to a more uniform refinement of the structure, resulting in less segregation and, consequently, reduced variation and improved stability.

## 6. Establishing a Common Line for Liquid-Phase and Semi-Solid Die Casting

Figure 14 shows the common line established by Aisan Industry for both liquid-phase and semi-solid die casting.

The area surrounded by dotted lines represents the existing die casting line, while the area surrounded by solid lines represents the process line exclusively for producing semi-solid slurry. In semi-solid die casting, the exclusive process line is fully automated, with robotic transport used for cooling the container,

**Figure 14** Overview of the line



applying a mold release agent to the container, producing slurry through vibration, and performing other processes.

In this way, establishing a common line has contributed to a reduction in investment and allowed production facilities to be effectively utilized according to production loads, thereby reducing costs.

## 7. Effects of the Development

Lastly, the effects of the development are summarized, as shown in Figures 15 and 16.

The first effect is the improvement of internal quality. Semi-solid die casting can reduce the void ratio to one-tenth of that in liquid-phase die casting. It was confirmed that semi-solid die casting helps reduce porosity, an internal defect, by preventing air entrapment and shrinkage, which are key characteristics of

**Figure 15** Improvement in internal quality

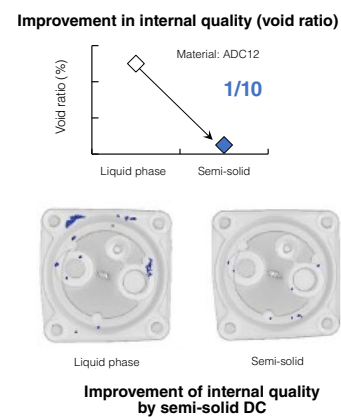
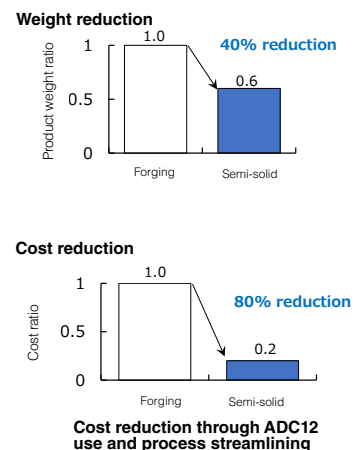


**Figure 16** Downsizing and cost reduction effects



this casting method.

The second effect is the facilitation of downsizing. Semi-solid die casting achieves approximately 40% reduction in weight compared to conventional forged components by ensuring fluidity and achieving near-net-shape production, similar to products made through liquid-phase die casting.

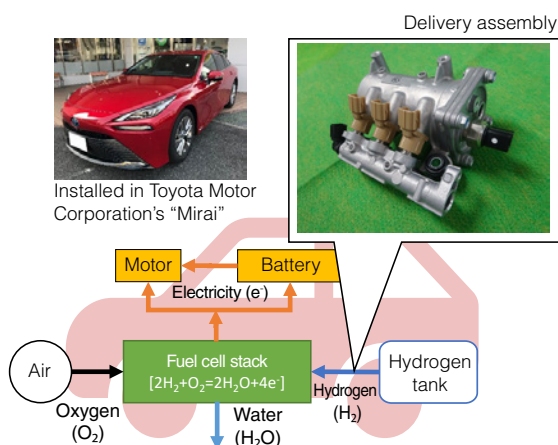
The third effect is cost reduction. Establishing a common line for liquid-phase and semi-solid die casting using ADC12 has reduced production costs by approximately 80% compared to forging. Additionally, using ADC12 can eliminate the need for T6 treatment, thereby contributing to a reduction in CO<sub>2</sub> emissions.

## 8. Conclusion and Future Actions

This development achieved the successful production of a semi-solid slurry of an alloy like ADC12, with a composition close to the eutectic point, which has been considered difficult. The developed technology for producing semi-solid slurry is now available for most alloys.

By using this technique and receiving significant cooperation from the individuals involved, we have achieved mass production of the second-generation hydrogen delivery assembly for FCVs (see Figure 17).

Figure 17 Hydrogen delivery assembly for fcvs



This research was conducted as part of the “Aichi Priority Research Project” initiated by Aichi Prefecture. We would like to express our profound gratitude to Kenji Miwa, a former staff member of the National Institute of Advanced Industrial Science and Technology (AIST), and Yuichiro Murakami, a staff member of AIST, for their cooperation in the project.

### Reference:

- Yuichiro Murakami, et al., Effects of Mechanical Vibration Factors on Size and Shape of Solid Particles in JIS AC4CH Aluminum Alloy Semi-Solid Slurry, Foundry Engineering, 86(9), (pp.728-733) (2014)
- Yuichiro Murakami, et al., Fluidity Evaluation of JIS AC4CH Aluminum Alloy Semi-solid Slurry made by Mechanical Vibration Method, Foundry Engineering, 86(10), (pp.773-780) (2014)
- Y. Murakami, et al., Non-Equilibrium Phase Crystallization of Al-Si Alloy Close to Eutectic Composition by Mechanical Vibration, Materials Transactions 63(12) (2022) (pp.1657-1661)
- Y. Murakami, et al., JIS ADC12 Aluminum Alloy Semi-Solid Slurry Preparation Technology by Applying Mechanical Vibration, Materials Transactions 95(1) (pp.16-22) (2023)
- Y. Murakami, et al., Effect of Injection Conditions in Semi-solid Injection Process

on Fluidity of AC4CH Aluminum Alloy, Materials Transactions 84(11) (pp. 605-611) (2012)

Y. Murakami, et al., Effect of Injection Velocity on Distribution of Primary a-phase Particles in Semi-solid High Pressure Die Casting of JIS AC4CH Aluminum Alloy, Materials Transactions 85(10) (pp. 665-671) (2013)

Y. Murakami, et al., Effect of the shape of solid particles on the distribution of particles in jis AC4CH (A356) Aluminum alloy Semi-Solid High-Pressure die casting, Light Metals 2016, 2016, pp. 201-206.

Y. Murakami, et al., Effect of Casting Condition in Semi-Solid Aluminum Alloy Injection Process on Distribution of Defects and Density, Shape Casting (2014) 11-18.

Y. Murakami, et al., Development of Slurry Preparation Method by Applying Mechanical Vibration, Solid State Phenomena 285 (2019) 333-338.

Y. Murakami, et al., Effect of Solid Particles on Fluidity of Semi-Solid Aluminum Alloy Slurry, Light Metals 2012 (2012) 297-301.

Y. Murakami, et al., Evaluation of fluidity of semi-solid aluminum alloy slurry prepared by mechanical vibration, 71st World Foundry Congress: Advanced Sustainable Foundry, WFC 2014, 2014.

Y. Murakami, et al., Effect of vibration conditions and shear rate on the shape of solid particles in JIS AC4CH aluminum alloy slurry made by applying mechanical vibration, 72nd World Foundry Congress, WFC 2016, 2016.

### Author Introduction



### Award-Winning Achievements

#### FY2021

- Aichi Invention Commendation: Aichi Invention Award (Aichi Prefecture Invention Association, a General Incorporated Association)
- Chubu Region Invention Commendation: Invention Encouragement Award (Japan Institute of Invention and Innovation, a Public Interest Incorporated Association)

#### FY2023

- Japan Foundry Engineering Society: Toyota Award (Japan Foundry Engineering Society, a Public Interest Incorporated Association)
- Sokeizai Industry Technology Award: Encouragement Prize (SOKEIZAI Center, a General Incorporated Association)
- Chubu Science and Technology Center Commendation: Promotion Prize (presented by the Public Foundation of Chubu Science and Technology Center, a Public Interest Incorporated Association)



# Motor Controller for Small Mobility

Tomoya Tanaka, Ryo Kojima, Yoshihiko Kawasaki, Yasuo Hosokawa, Shigemichi Ujiie

## Precise control maximizes the potential of electric mobility!

We are committed to technological development to make electric mobility more comfortable and efficient. Motors that power electric mobility do not move as intended just by drawing current from the battery. This is where the “motor controller” comes into play! It finely adjusts the current and frequency according to driving conditions—ensuring a smooth ride and fulfilling the user's intentions.

Aisan Industry has spent many years cultivating control technologies for engines and hybrid vehicles. Leveraging this experience, we develop hardware and software, as well as propose systems that perfectly match our customers' needs.

In addition, simulation technology is used to ensure lean designs and high-quality manufacturing processes. We

continue to make fine adjustments even after installation in vehicles to ensure optimal performance.

This technology reduces vehicle shaking when starting or driving at low speeds and prevents the vehicle from rolling backward when starting on a slope. We will continue to support the evolution of safe and comfortable mobility, taking on the challenge of creating new value!

### Highlights of Achievements

## 01

### Motor controller

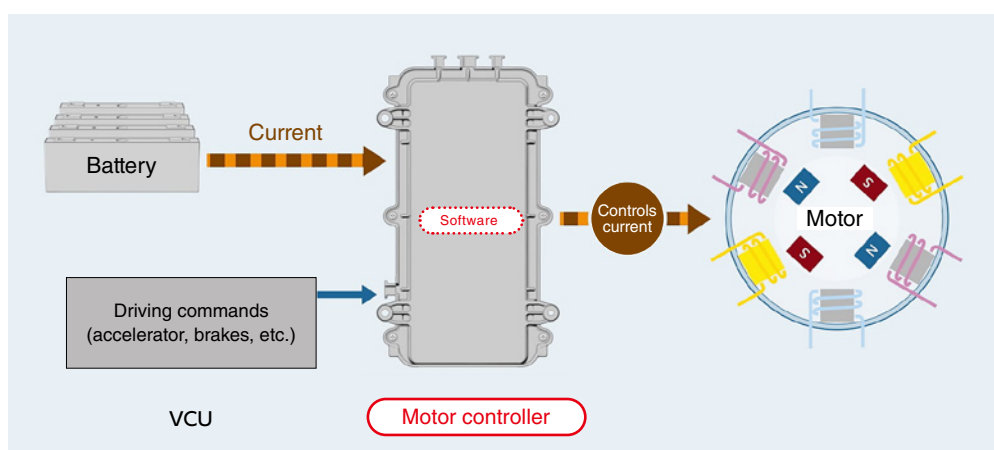
Motor controllers are essential products that support the entire mobility powertrain. They enable efficient driving by precisely controlling the current and frequency supplied to the motor according to driving conditions. This reduces mobility's acceleration and deceleration, as well as battery consumption.

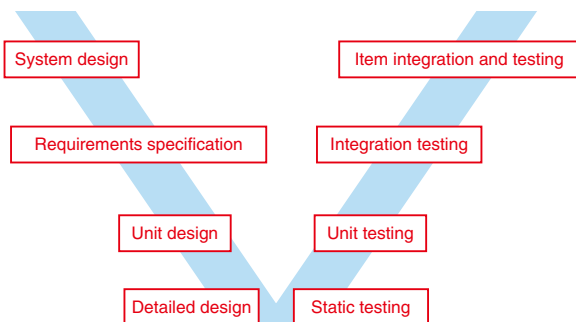


Circuit board required for motor control



Software

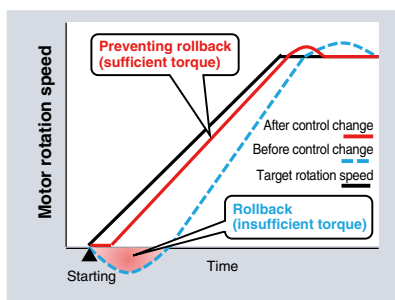
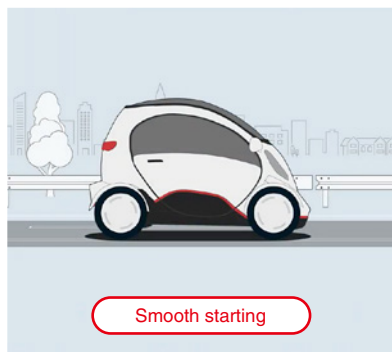




## 02

### V-shaped model process

Leveraging our many years of experience in engine and hybrid control development enables us to proceed with development systematically, according to process, and ensure high quality.

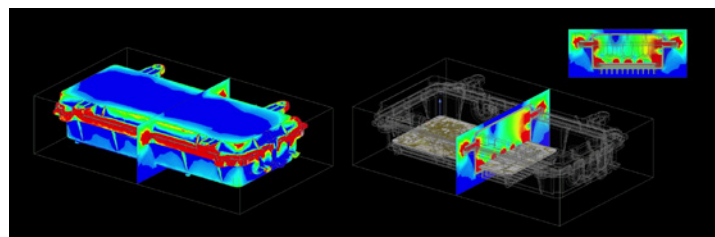


## Results (Problem Solving)

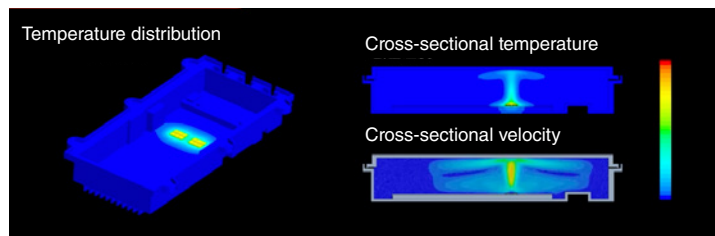
- Reduced shaking when starting to achieve a more comfortable ride.
- Prevented backward movement when starting on slopes, improving safety.

## Achievements

- We aim to promote the adoption of electric mobility further by continuing to pursue improvements and cost reductions.



Noise simulation



Thermal fluid analysis

## 03

### Simulation

We have shortened schedules and reduced prototyping costs by utilizing simulation in the design process to promote efficient development without rework.

## 04

### Motor control development

Our control technology and vehicle expertise, cultivated through body and torque control during hill starts, enable performance levels that meet mobility requirements.

# Deep Drawing Technology Development for BEV Battery Cases

Masayuki Tsukamoto, Keisuke Wakasugi

## Establishing a high-quality, thin-wall pressing method improves battery quality and reduces costs

As interest in environmental issues grows, the shift toward electric vehicles (EVs) is gaining momentum. In response, Aisan has developed manufacturing methods for lithium-ion battery cases for battery electric vehicles (BEVs). While battery cases are usually cylindrical or rectangular, we have successfully developed a rectangular case (01) that is strong, durable, and lightweight to meet the specific needs of our customers' in-vehicle applications. We achieved this by forming a single aluminum alloy sheet into the desired shape using deep drawing press technology (02).

In addition to applying simple deep drawing on sheet metal, the technology used to manufacture rectangular cans requires corner bending processing to form right angles. Furthermore, to ensure strength and durability, each side of the can requires a different sheet metal thickness. In response

to rising aluminum prices, it was necessary to create these shapes and ensure a high yield rate (the ratio of finished products to raw materials input) for aluminum.

To address these issues, Aisan introduced the "ironing press method," which utilizes the material's characteristics. Unlike conventional method that gradually deep draw the sheet material in multiple processes (if drawn all at once, it will crack and the desired shape cannot be achieved), our pressing method (03) reduces the number of processes and improves material yield. Furthermore, we pursued the optimal number of processes (03+) by incorporating a process design that suppresses cracking, as well as press tryout and CAE\* analysis.

\*Computer-aided engineering: design support using computers

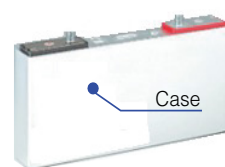
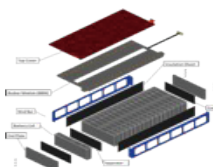
### Highlights of Achievements

## 01

### Rectangular shape

We have adopted a rectangular shape that offers high strength and durability while remaining lightweight to meet our customers' in-vehicle needs.

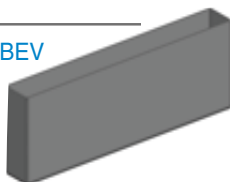
**Battery pack** Battery control **Battery module** Bundling battery cells **Battery cells** Charging section



Development model

Battery case for BEV

High-strength aluminum deep drawing  
W:308, D:40, H:100



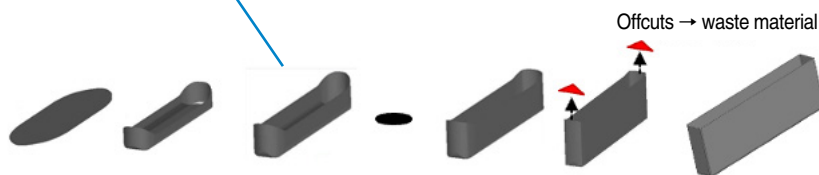
<Function and needs>

- Strength and durability:  $\pm 10\%$  plate thickness tolerance on each of the five sides
- Cost reduction through thinning and reducing material yield

## 02

## Deep drawing press

A single aluminum alloy sheet is formed into a rectangular shape through deep drawing press.



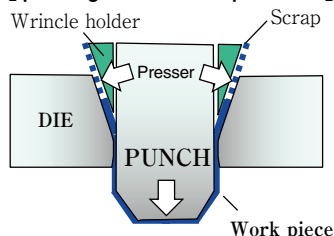
High-strength aluminum sheet → Manufacturing through multiple processes (molds) → Rectangular can

## Key points in pursuing MONOZUKURI

- ◎ Waste reduction:  
high material yield (more than 80%)
- ◎ Reduction in number of processes

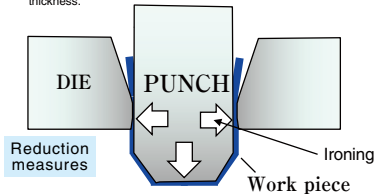
## In order to improve material yield

## [ Conventional: deep drawing while pressing down the workpiece ]



## [ Development: applying ironing force and stretch ]

Reducing the gap between the die and punch increases ironing force, which results in a large change in plate thickness.



Less scrap means an improved yield and fewer processes

## 03

## Ironing press method

We have introduced the "ironing press method" among deep drawing press methods that utilize the fact that the elongation rate of materials increases when they are stretched while compressive force is applied in the direction of the high plate thickness. Unlike conventional methods that deep draw the plate material gradually in multiple processes (if drawn all at once, it will crack and the desired shape cannot be achieved), this method has reduced the number of processes and improved material yield.

## 03+

## Pursuing the optimal number of processes

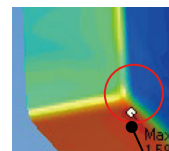
We determined the optimal number of processes by incorporating a process design that suppressed cracking, as well as press tryout and CAE analysis.

## Cracking



Reducing the number of processes too much (i.e., increasing the amount of deformation per process) can cause cracking

## Reduced stress concentration at corners



After improvement



Identified stresses that do not cause cracking through CAE analysis

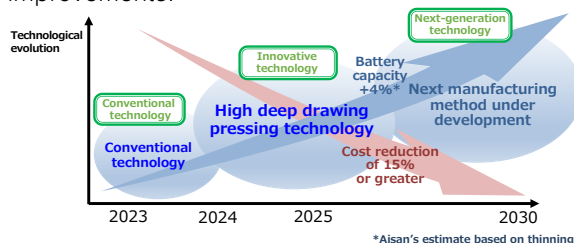
Successfully determined the process (mold) that suppresses cracking.

Results  
(Problem Solving)

- Contributed to increasing battery capacity and reducing costs (expected cost reduction of 5%).
- Saved energy through reduction in the number of processes (expected reduction of 140 tons of CO<sub>2</sub> per year).
- Achieved development that ensures high quality, along with safety and durability.
- Currently promoting initiatives with a view to mass production.

## Future Developments

- We are developing a new manufacturing method that will increase battery capacity as well as reduce costs by more than 15%, allowing us to make further improvements.



# Developing Software Engineers for Vehicle Electrification

Electric System Development Department

## Reskill Internal Talent to Drive the Future of the Automotive Industry!

Software engineers are essential for developing electric systems, the key to achieving carbon neutrality. However, Aisan has an extreme shortage of software engineers. We have primarily manufactured mechanical parts for engines, so we are not well-positioned to fill this need. There is also a shortage of talent in the industry as a whole, which has made it difficult to secure talent.

Therefore, in FY2022, we launched the “Software First 100 Project”(SWF100) with the goal of developing 100 software engineers over three years. We reskilled young and mid-career employees seeking to transition into software engineering, and provided training for new hires entering software development roles.

First, we formed a special task team for implementing development curriculums. We started by defining the type of talent Aisan sought. Then, we define the ideal goal for

engineers, Talent Development Policy, goals, and methods. As we implemented the Talent Development curriculums, we continuously refined our methods to enhance their effectiveness.

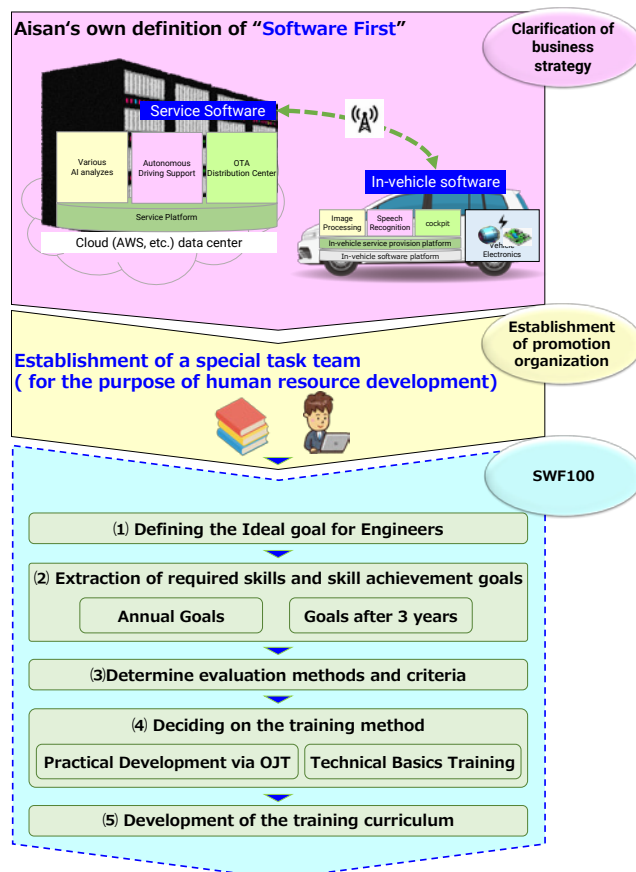
The development policy, outlined in section 01, involved making the skill acquisition status visible, selecting relevant topics, and providing guidance that considered the skill areas needing improvement and each individual's aptitude. By the final year of the program, the participants had grown to the point where they could contribute to the development of actual products under a leader's guidance. The three-year program ended in FY2024. We achieved nearly all of our goals in terms of participant numbers and skill levels. Going forward, we plan to focus on strengthening our organizational capabilities and cultivating leaders.

### Highlights of Achievements

## 01

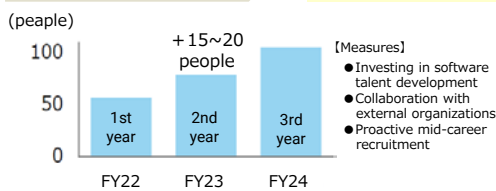
### Established Skill Development Goals and Methods Aligned with the Ideal Engineer Profile

In the planning phase, we first defined the ideal goal for engineers, the skill achievement goals for the next three years, the evaluation methods, and the development of the training curriculum. We defined the talent profile as “talent with the skills to independently develop in-vehicle systems,” based on the technologies in which Aisan Industry has traditionally excelled, plus software skills.

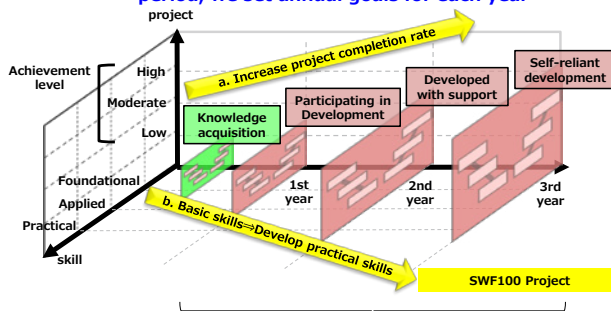


The core functions and added value of EV's are shifting toward software

Development of around 100 high-potential software engineers



To develop self-reliant engineers over a three-year period, we set annual goals for each year



Build real-world development skills through on-the-job training

## 02

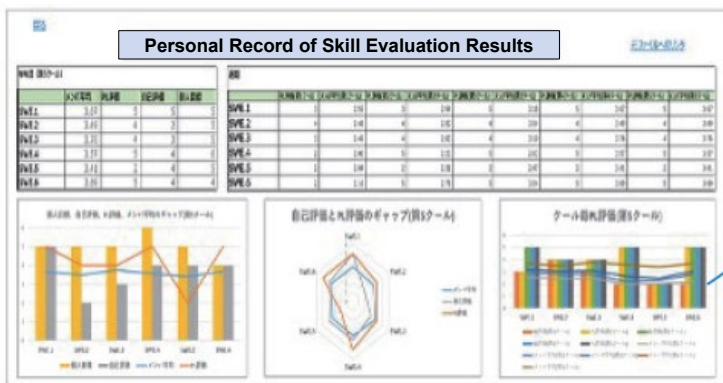
### Driving Practical Skill Development Through a Hands-On, OJT-Focused Curriculum

The development curriculum focused on on-the-job training (OJT) to quickly develop practical skills. Basic skills required for OJT are acquired through a three-month basic development of the training curriculum conducted prior to OJT. Development themes are set based on the business strategy roadmap. Each team advances development under the guidance of a project leader in accordance with the Aisan development process. Participants aim to enhance their skills by repeatedly experiencing development cycles called "season" every six to nine months.

		1st season Elemental Technology Development 2022/07-12	2nd season Real Theme Development 2023/01-06	3rd season Mass production preparation 2023/07-12	4th season Mass production preparation 2024/01-09	5th season Mass production preparation 2024/10-03
CN	Device Control					
	Drive Control					
E	Power Conversion Power Control					
	Power supply Power management					
common PF	Communication PF					
	Control PF					
CAS	Autonomous Driving					
	Service OUT-CAR					

Virtual product development

Real product development



## 03

### Development Status Monitoring and Timely Follow-Up

Member evaluations are visualized based on predefined criteria, and follow-ups are conducted according to individual aptitude.

The criteria are applied by expanding the industry standard ETSS (Embedded Technology Skill Standards).

### Results

- In three years, nearly all of the reskilled members advanced to the intermediate level they were aiming for.
- From the second half of FY2022 onward, they participated in multiple actual product development themes.
- Completed construction of a basics training and OJT curriculum system.

### Future Measures

- We will improve our capabilities to respond to new demands, such as increased development of mass production and in-vehicle security, as well as environmental changes, such as SDV and generative AI.
- Our key activities will focus on strengthening our talent (Development of Project Managers and Technical Experts, etc.) and our organization (High-quality development processes, management system utilization, etc.). Additionally, we will also accelerate the development of electrified products as a new project.

# MBD Promotion Through Model Libraries

Takahiro Nakamura, Yusei Noguchi

## Accelerated development by leveraging MBD! Enhanced development capabilities achieved

We worked on MBD (model-based development) to develop and verify models on computers. However, since each department worked on MBD separately, there were drawbacks, such as the duplication of model development. From 2020 to 2021, we conducted activities to standardize MBD and create a system that would allow models to be utilized as assets by the entire engineering department.

This was driven by the rapid changes in the automotive industry environment, such as CASE. To accelerate our response to electrification (E), one of the CASE elements, we strengthened our development capabilities and aimed to achieve mass production of electrified products at an early stage.

In order to develop internal combustion engine (engine-related) products while also developing electrified products, it is essential to improve design efficiency and development speed. Therefore, we promoted the use of MBD within the company to reduce rework and improve development speed. The issue of duplicated model development was resolved by creating a cloud-based storage location (model library) and standardizing the specifications (instruction manuals) format. This has achieved visibility of the model list. Additionally, establishing rules for model construction, such as naming conventions, has made interdepartmental reuse of models easier and resulted in numerous achievements.

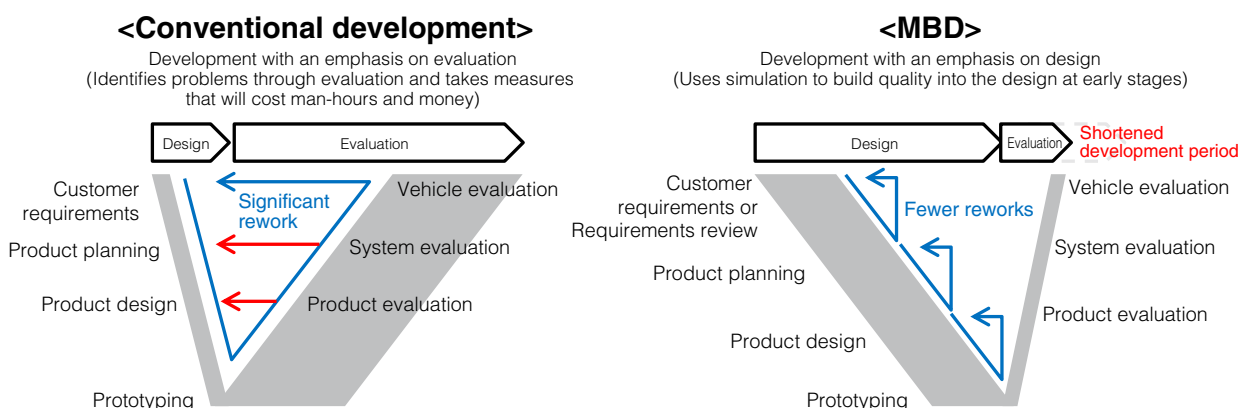
### Key Points of Development

## 01

### Development method using MBD

Using MBD makes it possible to use simulation in the early stages of design, implement small PDCA cycles, and build quality in the virtual world.

### Aiming to accelerate development using MBD



\* Excerpt: Modified from the Ministry of Economy, Trade and Industry's "strategic committee for the new era of automobiles (first meeting) materials" to align with Aisan Industry

## <Model storage location (model library)>

Listed by product, granularity, and software used  
⇒ Emphasizes ease of viewing and searching

	Granularity C	Granularity B	Granularity A
Granularity	Low		High
Motor			
Battery			
Control			

■ : Software A  
○ : Software B

Granularity: Degree of reproduction of actual machine

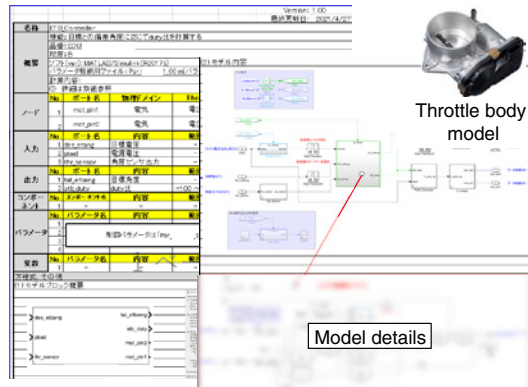
## 02

### Visualization of the development list

We created a model library that emphasizes ease of viewing and searching, as well as model specifications that can be used to record necessary information. This made it easy to visualize the developed models. We also reduced man-hours by utilizing similar models.

## <Model specifications (instruction manuals)>

Model information (input/output, calculation details, granularity), etc.

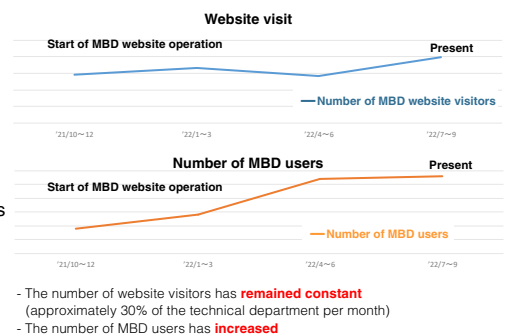


## 03

### MBD website

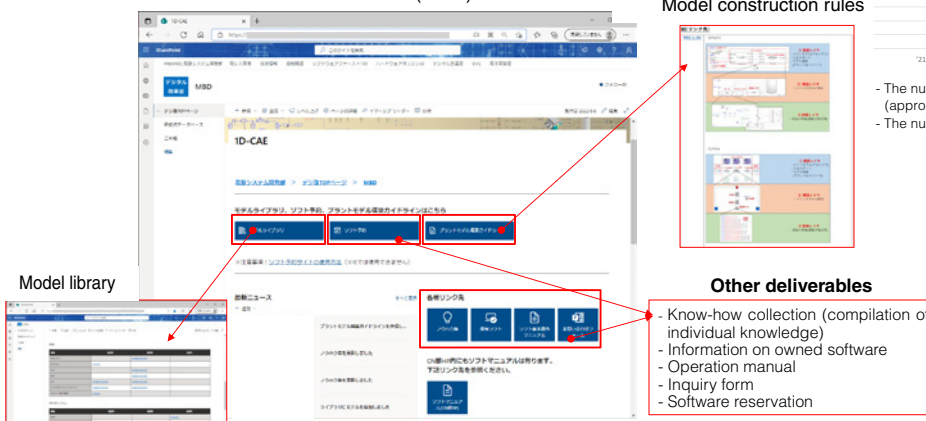
Through technical skills development, we are promoting the company-wide adoption of MBD. We have also built and operate an MBD website that aggregates all MBD-related information in the cloud.

## <Confirmation of the effectiveness of promoting MBD>



MBD website (cloud)

Model construction rules



## Results (Problem Solving)

- Created a model library to avoid duplication in development.
- Established model construction rules to enable the construction of standardized, easy-to-reuse models.
- Increased the number of MBD users by providing basic technical skills.

## Future Developments

- We will further enhance our model library to strengthen our development capabilities.

# Solenoid Valve Development Through Coupled Analysis

Takahiro Nakamura, Hiroki Kobayashi

A significant reduction in design period is achieved through the coupling of electromagnetic field analysis software with design exploration software or 1D-CAE software

There is a growing global movement toward carbon neutrality, which aims to offset greenhouse gas emissions and achieve a net-zero total, as well as toward a decarbonized society. In addition to renewable energy sources, such as solar and wind power, hydrogen is receiving considerable attention as an alternative to fossil fuels.

Since the mid-1990s, Aisan has been working on hydrogen-based products, some of which have been adopted by the "MIRAI," a car that does not emit carbon dioxide and is attracting attention as the ultimate eco-friendly vehicle. We have now taken on the challenge of developing a new linear solenoid valve (LSV) to expand our line of products for fuel cell vehicles (FCVs).

The LSV is a device that adjusts fluid flow using an

electric current. However, it often needs to be examined repeatedly during the magnetic circuit design process, which has made developing it challenging. To address this issue, we used a coupling method based on JMAG electromagnetic field analysis software. We automated the optimal design of the entire product by examining its shape through coupling with design exploration software. We also developed an analysis method that evaluates responsiveness by coupling it with 1D-CAE\*. These two new design methods reduced the design period by 68% and achieved a 20% reduction in product size.

We intend to systematize the construction techniques for design methods cultivated through this challenge and apply them to new challenges.

\*Design support concepts, methods, and tools that are applicable from the upstream stage

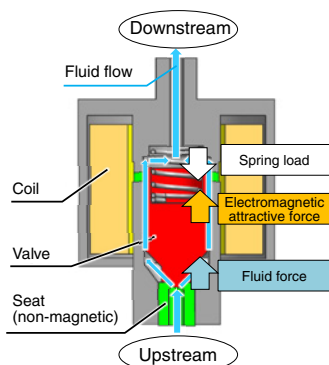
## Highlights of Achievements

## 01

### Two issues and countermeasures

There were two major issues, one of which was that coil specifications (wire diameter, etc.) and magnetic circuit shape were examined separately, often resulting in repeated rework.

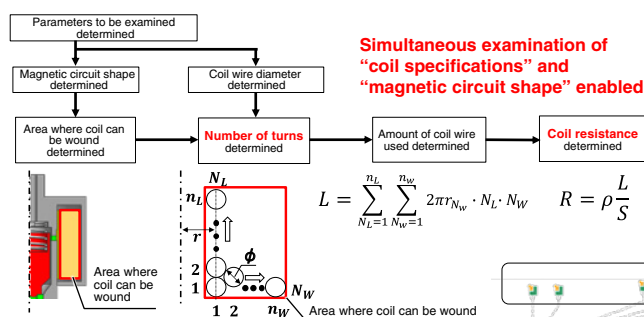
#### <LSV>



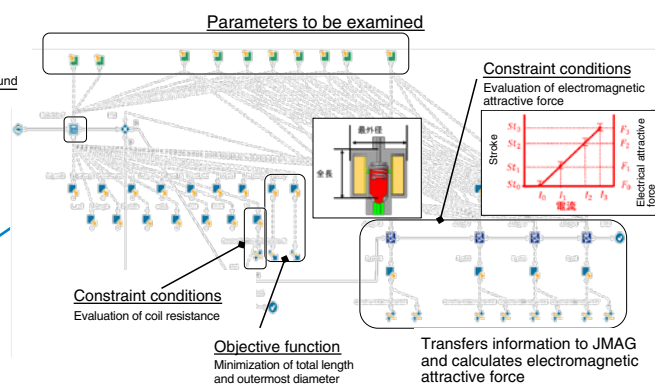
#### <Solving issues using JMAG>

	Issue 1	Issue 2
	Separately examining "coil specifications" and "magnetic circuit shape" resulted in failure to achieve optimal design for the product as a whole	Transient loads were not formulated, making it impossible to predict performance until actual measurements are taken
Implemented measures	<b>Coupling JMAG with design exploration software</b> ⇒ Optimizing the design of the entire product by simultaneously exploring "coil specifications" and "magnetic circuit shape"	<b>Coupling JMAG with 1D-CAE</b> ⇒ Building a model to calculate transient loads to ensure analytical accuracy that can be used for evaluation

## <Calculation of coil specifications>



## <Design exploration model>



# 02

## Coupling with design exploration software

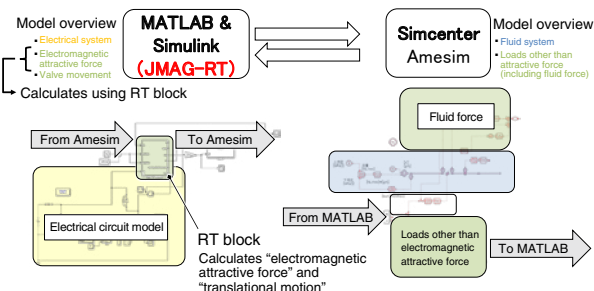
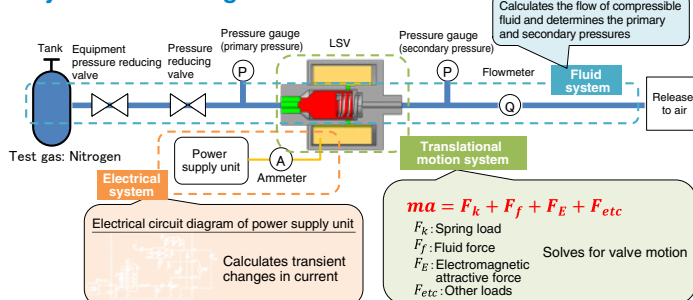
The design exploration software determines the shape dimensions, which are then transferred to JMAG. The analysis model is automatically generated using the Shape Editor function. Using design exploration reduced the magnetic circuit design period by 89%.

# 03

## Coupling with 1D-CAE

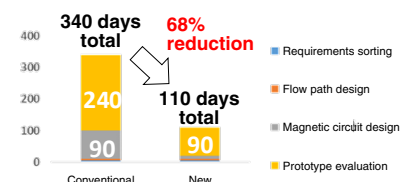
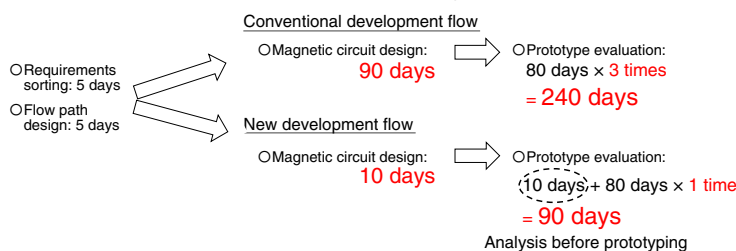
We conducted a response evaluation based on the shapes obtained in 02 (coupling JMAG with design exploration software). The model was created using 1D-CAE to analyze three physical domains: electrical, fluid, and translational motion systems.

## <System block diagram>



## Results (Problem Solving)

- Built two design methods using JMAG's coupling technology.
  - Shape examination through coupling with design exploration software
  - Response evaluation through coupling with 1D-CAE
- The optimization of the design of the entire product resulted in a 20% reduction in both the overall length and the outermost diameter.
- Improved the development flow and reduced the design period by 68% (from 340 days to 110 days), as well as development costs by 67%, by decreasing the number of times a prototype is made (from three to one).



## Future Developments

- We will apply the analysis technology that we developed this time to other products.
- We will continue developing new analysis technologies aiming to further improve efficiency.

# Join the Intellectual Property Business Matching Projects

Intellectual Property Sect. Corporate Planning Dept.

## Licensing drone patents intended to create new value and support other businesses

Many new patents are filed every year, but even after obtaining the rights, many patents remain unused and dormant. In Japan, there are approximately 1.6 million patents, half of which are reportedly unused, and these are held by large enterprises. The "Intellectual Property Business Matching" project connects these unused patents with small and medium-sized enterprises and startups to develop attractive products and create new businesses.

We are actively participating in this project from the perspective that combining our patents with the ideas and technologies of external personnel will lead to the creation of new value, and from the perspectives of social contribution and enhancing corporate value. We are providing drone-

related patents and designs patents to platforms operated by the Ministry of Economy, Trade and Industry (Kansai Bureau of Economy, Trade and Industry), Aichi Bank, and Nikkan Kogyo Shimbun. Aisan's drones are hybrid-powertrain and utilize engine technology cultivated through the development of automotive parts. They feature significantly longer flight ranges than electric drones. We plan to publicly disclose the drone-related patents of flight control and design patents obtained through this drone development as licensable patents\*, in the hope that they will support companies considering developing or manufacturing drones or flying cars.

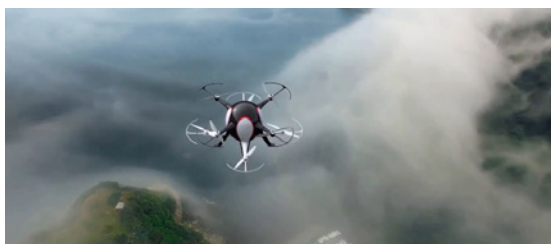
\*Patents that the applicant intends to license to others through a license agreement, etc.

### Key Points of the Licensable Patents

#### <Technical features>

During hovering flight, the drone is driven at a predetermined output value. This value is higher than the minimum required for hovering flight, but lower than the minimum required for ascending flight. This enables long flight times by charging excess power to the battery. [Output Control]

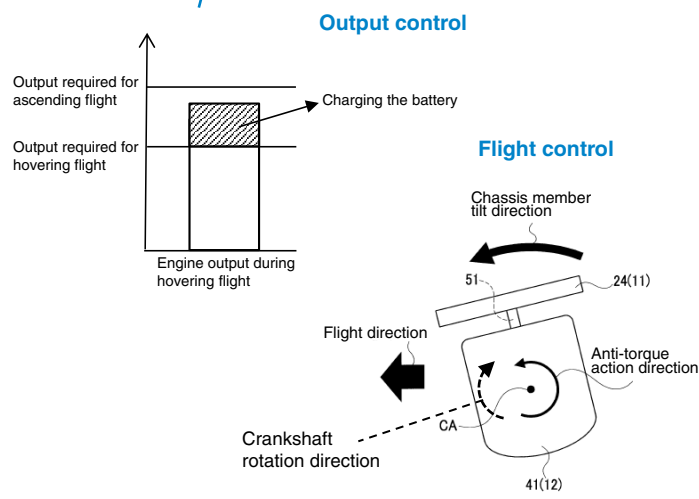
During mobile flight, the drone's tilt direction (traveling direction) is aligned with the direction of the anti-torque generated by the engine to achieve energy-efficient flight. [Flight Control]



## 01

### Patents related to drone control

These patents relate to output and flight control, which enables long flight times and energy efficiency.

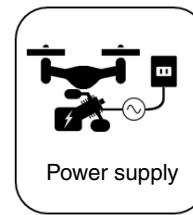
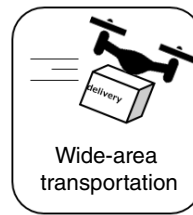


### <Examples of potential applications>

Hybrid drones and flying cars, which are powered by both engines and batteries.



### Examples of uses



## 02

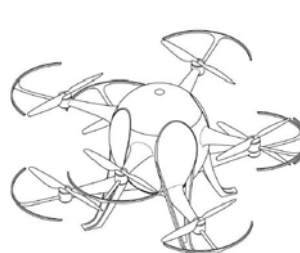
### Design patents concerning the external appearance of the drone

The concept is "to give people a sense of reassurance and kindness," and its design features set it apart from typical drones.



### <Design patents features>

- Egg-shaped design to convey softness
- Gentle and safe transportation image, as if carrying eggs
- Curved frame design to prevent injury during use
- User-friendly height for easily handling cargo



Perspective view



Perspective view (lid open)

### <Design model examples>



## Results (Problem Solving)

- We have listed the patents and design patents as licensable patents on the platform of the Ministry of Economy, Trade and Industry (Kinki Bureau of Economy, Trade and Industry), Aichi Bank, and Nikkan Kogyo Shimbun.

## Future Developments

- We would like to make this project available on platforms other than the ones currently provided.
- If there are requests to use the patents, we would like to actively support their commercialization.
- In the future, we would like to make technologies other than drones available as needed.



## Double Eccentric Valve for EGR Systems

### 1. Overview of the Invention, etc.

The present invention is used in automobile engine exhaust gas recirculation (EGR) valve systems, where it contributes to cleaning the exhaust gas and improving fuel efficiency. EGR refers to a system that returns a portion of the exhaust gas emitted from the engine back to the intake side for re-combustion. Originally, EGR was mainly used for exhaust gas purification (NO<sub>x</sub> reduction) in diesel vehicles. However, since EGR reduces intake resistance and fuel consumption, it is now widely used in gasoline vehicles as well. (Figure 1)

Compared to conventional EGR valves (Conventional product 1 in Figure 2), the present invention nearly doubles the recirculation flow rate without enlarging the product. This contributes to reducing the weight of automobiles and their environmental impact.

Currently, the present invention is produced domestically at a rate of approximately 600,000 units per year for domestic supply.

Figure 1 Exhaust gas recirculation system and EGR valve

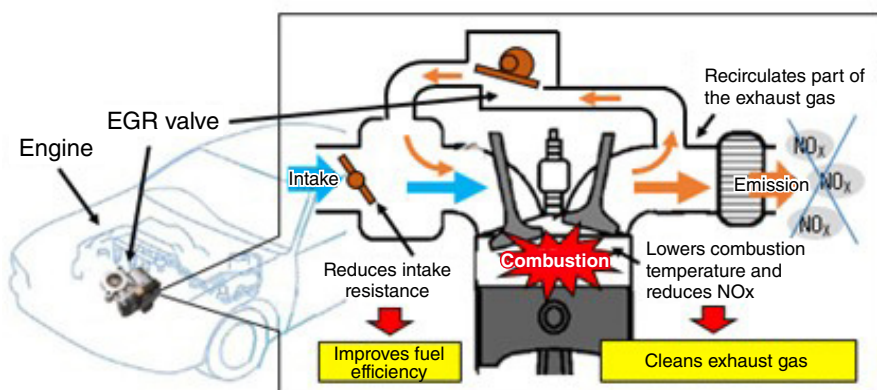
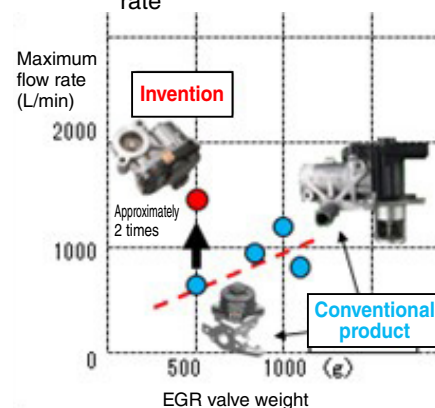


Figure 2 Relationship between product weight and maximum flow rate



### 2. Issues with Conventional Inventions and Development Needs

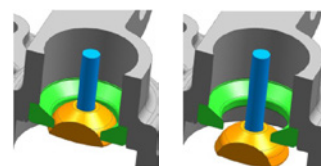
Conventional EGR valves were primarily poppet valves (small size, low flow rate, and high sealing). However, as the amount of recirculated exhaust gas (EGR rate) increases, fuel efficiency and exhaust gas cleanliness improve. Therefore, there has recently been a demand for high flow rates of recirculated exhaust gas. Various companies have proposed the following improvements to achieve high flow rates. (Figure 3)

To meet the development needs for high flow rates, it was difficult to commercialize conventional product 2, and conventional product 1 required enlargement, which would increase its weight.

Figure 3 Conventional technologies and their issues

#### Conventional product 1 (poppet valve)

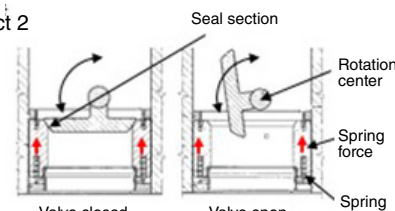
- High sealing and miniaturization are possible for small flow rates
- High sealing is possible for large flow rates, but larger sizes are required



⇒ As flow rate increases, size also increases

#### Conventional product 2 (butterfly valve)

- Miniaturization and large flow rates are possible, but maintaining high sealing is difficult



⇒ The sealing section wears out due to the pressure exerted by the spring force, which makes maintaining the sealing level difficult

### 3. Features of the Invention, etc.

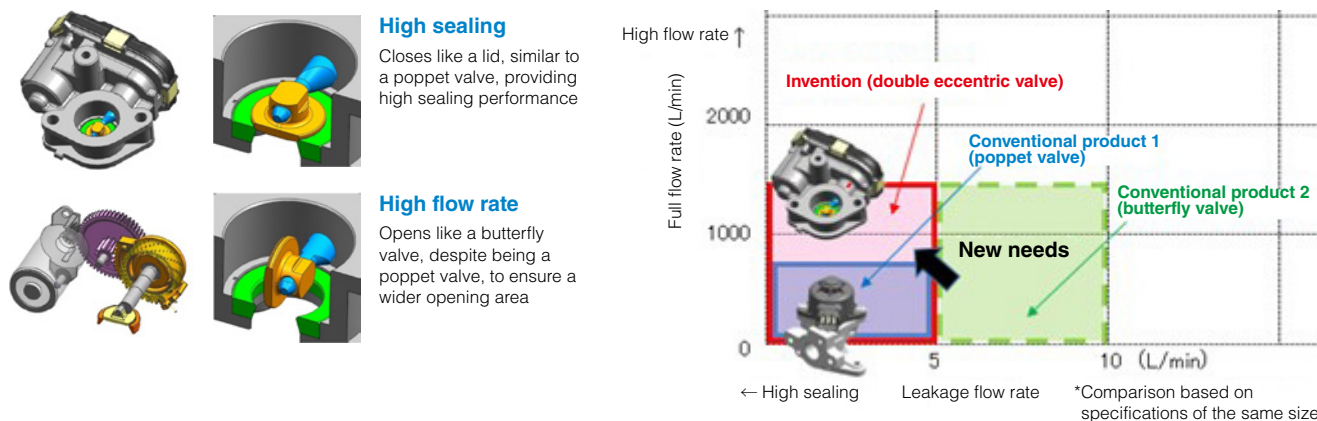
The present invention has a structure that achieves high flow rates and sealing performance without enlarging the product. By shifting the center axes of the shaft and valve left and right and up and down (double eccentricity), the product opens like a butterfly valve, which excels at high flow rates, and

closes like a poppet valve, which provides excellent sealing performance (Claim 1).

Furthermore, since the present invention relates to fundamental valve technology, it is expected to have various applications.

#### <Feature 1> Balancing conflicting performance requirements

Figure 4 Structure and performance of the invention (double eccentric valve)



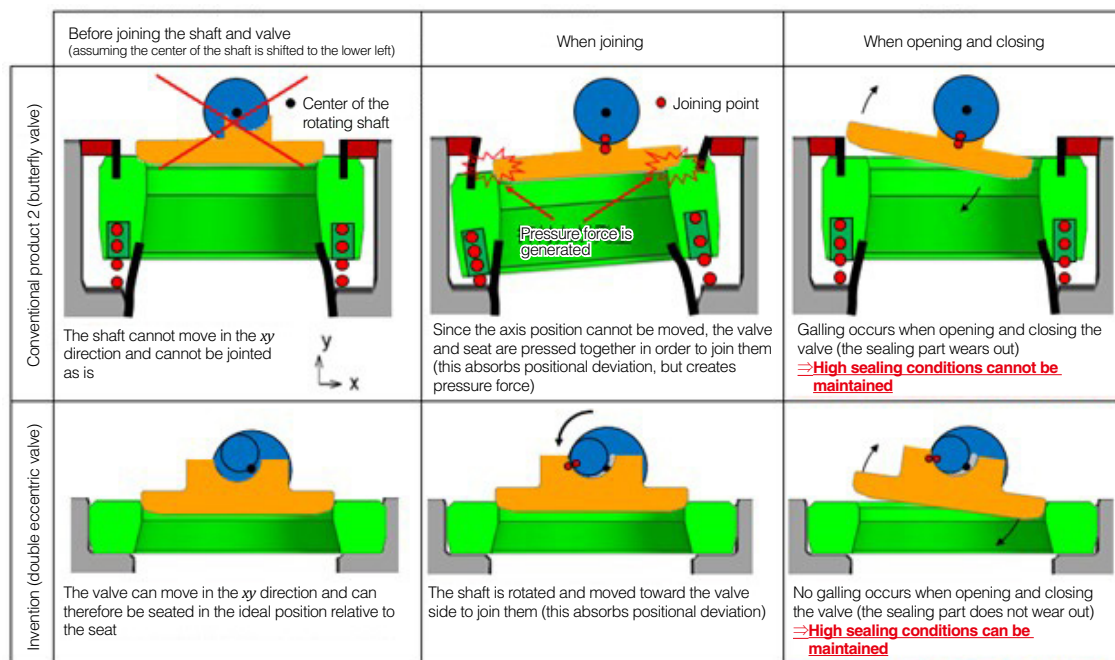
#### <Feature 2> Excellent durability and a simple structure

In the conventional product 2 butterfly valve (Figure 3, bottom), dimensional variations in each component were attempted to be absorbed by (1) the floating valve seat structure and (2) the pressure applied to the sealing section by the spring. However, with this structure, sealing performance is only ensured when the valve is new. The contact pressure between the valve body and valve seat inevitably increases during opening and closing of the valve, causing localized welding, or "galling," to occur. This results in wear of the sealing section, making it impossible to maintain a high sealing state. (Figure 5, top)

On the other hand, the double eccentric valve of the present invention utilizes (1) the eccentric shaft structure and (2) the gap between the shaft and the valve, absorbing variations in each component during assembly. Consequently, galling does not occur during opening or closing of the valve, and the sealing performance remains at the same level as when the product is new. (Figure 5, bottom)

Furthermore, when comparing the number of components around the valve, there are eight for the conventional product 2 while there are four for the invention, half as many.

Figure 5 Structural comparison between the invention and conventional technologies



## Award-Winning Achievements

### FY2020

Aichi Invention Commendation: Aichi Invention Award (Aichi Prefecture Invention Association, General Incorporated Association)

Chubu Region Invention Commendation: Invention Encouragement Award (Japan Institute of Invention and Innovation, a Public Interest Incorporated Association)

### FY2022

Chubu Science and Technology Center Commendation: Encouragement Prize (presented by the Public Foundation of Chubu Science and Technology Center, a Public Interest Incorporated Foundation)

### FY2024

Commendation for Science and Technology by the Minister of Education, Culture, Sports, Science and Technology: Science and Technology Award (Development Category) (Ministry of Education, Culture, Sports, Science and Technology)



## **AISAN INDUSTRY CO., LTD.**

1-1-1 Kyowa-cho, Obu, Aichi 474-8588 Japan  
<https://www.aisan-ind.co.jp/en/>